FERMILAB-PUB-20-020-A-AD-AE-SCD (accepted) DOI:10.3847/1538-3881/ab7002

Draft version January 20, 2020
Typeset using LaTeX **twocolumn** style in AASTeX62

arXiv:2001.06060v1 [astro-ph.EP] 16 Jan 2020

DYNAMICAL CLASSIFICATION OF TRANS-NEPTUNIAN OBJECTS DETECTED BY THE DARK ENERGY SURVEY

T. Khain,[1] J.C. Becker,[1] Hsing Wen Lin (林省文),[1] D. W. Gerdes,[2,1] F. C. Adams,[1,2] P. Bernardinelli,[3]
G. M. Bernstein,[3] K. Franson,[1] L. Markwardt,[1] S. Hamilton,[1] K. Napier,[1] M. Sako,[3] T. M. C. Abbott,[4]
S. Avila,[5] E. Bertin,[6,7] D. Brooks,[8] E. Buckley-Geer,[9] D. L. Burke,[10,11] A. Carnero Rosell,[12,13]
M. Carrasco Kind,[14,15] J. Carretero,[16] L. N. da Costa,[13,17] J. De Vicente,[12] S. Desai,[18] H. T. Diehl,[9] P. Doel,[8]
B. Flaugher,[9] J. Frieman,[9,19] J. García-Bellido,[5] E. Gaztanaga,[20,21] D. Gruen,[22,10,11] R. A. Gruendl,[14,15]
J. Gschwend,[13,17] G. Gutierrez,[9] D. L. Hollowood,[23] K. Honscheid,[24,25] D. J. James,[26] N. Kuropatkin,[9]
M. A. G. Maia,[13,17] J. L. Marshall,[27] F. Menanteau,[14,15] C. J. Miller,[2,1] R. Miquel,[28,16] A. A. Plazas,[29]
E. Sanchez,[12] V. Scarpine,[9] M. Schubnell,[1] I. Sevilla-Noarbe,[12] M. Smith,[30] F. Sobreira,[31,13] E. Suchyta,[32]
M. E. C. Swanson,[15] G. Tarle,[1] A. R. Walker,[4] and W. Wester[9]
The Dark Energy Survey Collaboration

[1] *Department of Physics, University of Michigan, Ann Arbor, MI 48109, USA*
[2] *Department of Astronomy, University of Michigan, Ann Arbor, MI 48109, USA*
[3] *Department of Physics and Astronomy, University of Pennsylvania, Philadelphia, PA 19104, USA*
[4] *Cerro Tololo Inter-American Observatory, National Optical Astronomy Observatory, Casilla 603, La Serena, Chile*
[5] *Instituto de Fisica Teorica UAM/CSIC, Universidad Autonoma de Madrid, 28049 Madrid, Spain*
[6] *CNRS, UMR 7095, Institut d'Astrophysique de Paris, F-75014, Paris, France*
[7] *Sorbonne Universités, UPMC Univ Paris 06, UMR 7095, Institut d'Astrophysique de Paris, F-75014, Paris, France*
[8] *Department of Physics & Astronomy, University College London, Gower Street, London, WC1E 6BT, UK*
[9] *Fermi National Accelerator Laboratory, P. O. Box 500, Batavia, IL 60510, USA*
[10] *Kavli Institute for Particle Astrophysics & Cosmology, P. O. Box 2450, Stanford University, Stanford, CA 94305, USA*
[11] *SLAC National Accelerator Laboratory, Menlo Park, CA 94025, USA*
[12] *Centro de Investigaciones Energéticas, Medioambientales y Tecnológicas (CIEMAT), Madrid, Spain*
[13] *Laboratório Interinstitucional de e-Astronomia - LIneA, Rua Gal. José Cristino 77, Rio de Janeiro, RJ - 20921-400, Brazil*
[14] *Department of Astronomy, University of Illinois at Urbana-Champaign, 1002 W. Green Street, Urbana, IL 61801, USA*
[15] *National Center for Supercomputing Applications, 1205 West Clark St., Urbana, IL 61801, USA*
[16] *Institut de Física d'Altes Energies (IFAE), The Barcelona Institute of Science and Technology, Campus UAB, 08193 Bellaterra (Barcelona) Spain*
[17] *Observatório Nacional, Rua Gal. José Cristino 77, Rio de Janeiro, RJ - 20921-400, Brazil*
[18] *Department of Physics, IIT Hyderabad, Kandi, Telangana 502285, India*
[19] *Kavli Institute for Cosmological Physics, University of Chicago, Chicago, IL 60637, USA*
[20] *Institut d'Estudis Espacials de Catalunya (IEEC), 08034 Barcelona, Spain*
[21] *Institute of Space Sciences (ICE, CSIC), Campus UAB, Carrer de Can Magrans, s/n, 08193 Barcelona, Spain*
[22] *Department of Physics, Stanford University, 382 Via Pueblo Mall, Stanford, CA 94305, USA*
[23] *Santa Cruz Institute for Particle Physics, Santa Cruz, CA 95064, USA*
[24] *Center for Cosmology and Astro-Particle Physics, The Ohio State University, Columbus, OH 43210, USA*
[25] *Department of Physics, The Ohio State University, Columbus, OH 43210, USA*
[26] *Center for Astrophysics | Harvard & Smithsonian, 60 Garden Street, Cambridge, MA 02138, USA*
[27] *George P. and Cynthia Woods Mitchell Institute for Fundamental Physics and Astronomy, and Department of Physics and Astronomy, Texas A&M University, College Station, TX 77843, USA*
[28] *Institució Catalana de Recerca i Estudis Avançats, E-08010 Barcelona, Spain*
[29] *Department of Astrophysical Sciences, Princeton University, Peyton Hall, Princeton, NJ 08544, USA*
[30] *School of Physics and Astronomy, University of Southampton, Southampton, SO17 1BJ, UK*
[31] *Instituto de Física Gleb Wataghin, Universidade Estadual de Campinas, 13083-859, Campinas, SP, Brazil*
[32] *Computer Science and Mathematics Division, Oak Ridge National Laboratory, Oak Ridge, TN 37831*

Corresponding author: Tali Khain
talikh@umich.edu

ABSTRACT

The outer Solar System contains a large number of small bodies (known as trans-Neptunian objects or TNOs) that exhibit diverse types of dynamical behavior. The classification of bodies in this distant region into dynamical classes – sub-populations that experience similar orbital evolution – aids in our understanding of the structure and formation of the Solar System. In this work, we propose an updated dynamical classification scheme for the outer Solar System. This approach includes the construction of a new (automated) method for identifying mean-motion resonances. We apply this algorithm to the current dataset of TNOs observed by the Dark Energy Survey (DES) and present a working classification for all of the DES TNOs detected to date. Our classification scheme yields 1 inner centaur, 19 outer centaurs, 21 scattering disk objects, 47 detached TNOs, 48 securely resonant objects, 7 resonant candidates, and 97 classical belt objects. Among the scattering and detached objects, we detect 8 TNOs with semi-major axes greater than 150 AU.

1. INTRODUCTION

Our Solar System harbors a large collection of small icy bodies that orbit the Sun beyond Neptune. In the past two decades, the number of these trans-Neptunian objects (TNOs) that has been discovered has grown to thousands. As these objects are believed to be primordial tracers of the early Solar System, the characterization of the trans-Neptunian population is vital for understanding and testing theoretical models of Solar System formation. For example, in one class of theories collectively known as the Nice Model (Tsiganis et al. 2005; Nesvorný 2011; Batygin et al. 2012), the starting orbits of the giant planets are different from those of the present epoch. Such models predict sizes and distributions of the different sub-populations of TNOs in the Kuiper belt due to the orbital migration of the larger planets to their current locations.

Over the past decades, a number of surveys intended to study the outer Solar System have significantly increased the population of known TNOs (e.g., Trujillo et al. 2001; Adams et al. 2014; Schwamb et al. 2010; Petit et al. 2011; Bannister et al. 2018), allowing these theories to be tested. Today, the growing number of observed objects combined with the development of survey simulators (Lawler et al. 2018; Hamilton & DES Collaboration 2019) allows for detailed comparisons of the observed and predicted populations (Volk et al. 2016, 2018) as expected within single modern surveys.

The trans-Neptunian objects themselves can be characterized in a variety of ways, including their size, color, and composition. These physical properties of the objects, however, are often difficult to observe. Fortunately, the orbits of the objects can provide insight into the structure and dynamical history of this distant region. By categorizing the TNOs based on their dynamical behaviors, we can extract information about the various sub-populations of the outer Solar System. The primary works that laid out this type of dynamical classification scheme are those of Elliot et al. (2005) and Gladman et al. (2008); the major dynamical classes of the Kuiper belt include the Neptune-resonant objects, centaurs, scattering disk objects, detached TNOs, and more (see below).

One of the surveys that has led to the discovery of these Kuiper belt objects is the Dark Energy Survey (DES) (Dark Energy Survey Collaboration et al. 2016), a nominal five year baseline optical survey intended primarily for cosmological purposes. DES used the Dark Energy Camera (DECam, Flaugher et al. 2015) on the 4-meter Blanco telescope at the Cerro Tololo Inter-American Observatory in Chile. Its survey area subtended a total of 5000 square degrees of sky, which was tiled with two survey modes: the Wide Survey, which imaged the full survey area roughly twice per year to a limiting magnitude of $r \sim 23.8$ mag for single epoch exposures in each of the *grizY* bands; and the Supernova Survey (Bernstein et al. 2012), which consisted of 30 square degrees spread over ten regions, each of which were imaged roughly weekly in the *griz* bands.

In a partial search of its first four years of data, DES has detected over two hundred TNOs (and counting). The discoveries so far include Neptune trojans (Gerdes et al. 2016; Lin et al. 2019), a dwarf planet candidate (Gerdes et al. 2017), two members of a potentially associated triplet family (Khain et al. 2018), and a high-inclination extreme TNO (Becker et al. 2018), with further publications detailing the results of additional analysis to come. Now that the current DES dataset has grown to this substantial size, it is of great interest to study the dynamical properties of this TNO population.

In this work, we present the dynamical classification of 240 trans-Neptunian objects detected by the Dark Energy Survey. Although the present application is to this particular set of TNOs, the classification scheme developed herein can be used more broadly. In Section 2, we lay out the different categories of TNOs and our classification algorithm, which differs somewhat from that of Gladman et al. (2008). In addition, we outline our

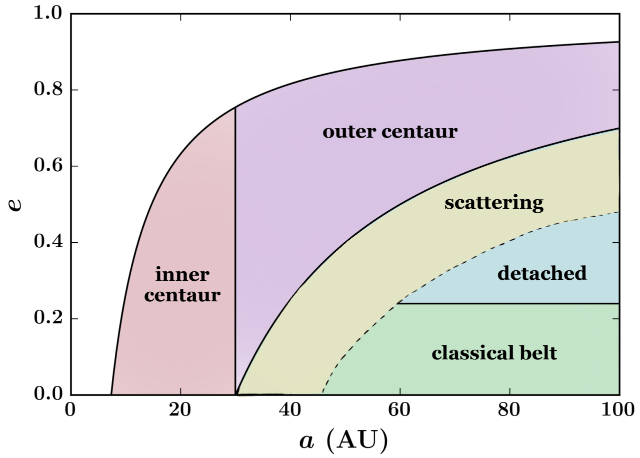

Figure 1. The dynamical classes of the outer Solar System. The black solid curves correspond to constant perihelion distances, with $q = 7.35$ AU and $q = 30$ AU (top to bottom). The inner centaurs (red region) have orbital periods less than Neptune's. The outer centaurs (purple) have orbits with perihelion distances below Neptune's orbit, but with semi-major axes outside the giant planet region. The scattering population (SDOs, scattering disk objects) mostly lies along the $q = 30$ AU curve and is shown in yellow. The classical belt (green region) and the detached objects (blue region) are removed from the Neptune scattering region, with the higher eccentricity detached TNOs above the classical belt. A companion plot with the DES TNOs on this phase plane is found in Figure 8.

newly developed resonance-finding method that allows for an automated resonance search without visual inspection. In Section 3, we apply this algorithm to the object sample and present the classification of the known DES TNOs. We discuss our results and their implications for future work in Section 4.

2. CLASSIFICATION METHOD

In this work, we apply the classification scheme of Gladman et al. (2008) with a few changes that reflect the development of the field in the last decade. The categories of objects and the definitions we adapt are described below and are visually represented in Figure 1. As with any classification scheme, a few of the category boundaries are rather arbitrary, as some of these dynamical properties lie on a spectrum. Deviations from Gladman et al. (2008) are denoted with an asterisk*.

Jupiter-coupled object. Jupiter-coupled objects are defined through the Tisserand paramater T_J with respect to Jupiter,

$$T_J = \frac{a_J}{a} + 2\sqrt{\frac{a}{a_J}(1-e^2)}\cos i, \tag{1}$$

where a_J is the semi-major axis of Jupiter, and a, e, i are the semi-major axis, eccentricity, and inclination of the object, respectively. Objects with $T_J < 3.05$ and perihelion distances below $q < 7.35$ AU are considered to be Jupiter-coupled objects.

Since the current DES sample does not contain any objects which exhibit cometary dynamics, we drop this category in future discussion of the classification results.

Centaur*. Centaurs are objects that experience strong interactions with the giant planets. In this work, we propose to separate this class into two: inner centaurs and outer centaurs. Inner centaurs (the traditional centaurs described in Gladman et al. 2008) are objects with semi-major axes smaller than Neptune's ($a < a_N \approx 30$ AU). We define outer centaurs to be objects with perihelion distances shorter than Neptune's semi-major axis ($q < a_N$), but semi-major axes larger than Neptune's semi-major axis ($a > a_N$).

Although both types of centaurs spend time within the giant planet region, the frequency of interactions with the planets differs for each class. The inner centaurs may experience strong interactions with the giant planets at most points on their orbit, while the outer centaurs are affected once an orbit, during perihelion crossing; moreover, the orbital period of an outer centaur is longer than of an inner centaur, resulting in fewer interactions per unit time. This distinction highlights the difference in the instability timescale: the outer centaurs are longer-lived objects than the short lifetime inner centaurs (Tiscareno & Malhotra 2003; Horner et al. 2004). By this classification, a traditional centaur such as Chiron (Kowal et al. 1979) falls into the inner centuar category, while longer-period objects with high eccentricity such as Drac (Gladman et al. 2009) or Niku (Chen et al. 2016) are deemed outer centaurs.

An example of the dynamics of inner and outer centaurs from the DES set is shown in Figure 2.

Oort cloud object. Objects in the Oort cloud are defined to have semi-major axes $a > 2000$ AU. Due to their large orbits, these bodies are most likely affected by galactic tides and passing stars. The present DES sample does not contain any objects in this class.

Resonant object. The outer Solar System consists of a large number of TNOs in mean motion resonances with Neptune. In order to be in a Neptune mean motion resonance, a TNO must be near an integer period ratio with Neptune's period, and must have a librating resonance argument of the form

$$\phi = p\lambda_N + q\lambda + r\varpi_N + s\varpi, \tag{2}$$

where $p, q, r,$ and s are integers that satisfy the d'Alembert relation, $p + q + r + s = 0$. Here,

$\lambda = \Omega + \omega + M$ is the mean longitude, $\varpi = \Omega + \omega$ is the longitude of perihelion, the subscript N refers to Neptune's orbital elements, and the non-subscripted variables refer to the TNO. Such a resonance is then referred to as a p:q resonance, the ratio of Neptune's orbital period to that of the TNO. In this work, we only consider the eccentricity-type resonances given by Equation 2, as was done in Gladman et al. (2008). In theory, TNOs could also experience inclination-type resonances, which include independent Ω and Ω_N terms. Since these are a higher order effect, we leave the study of inclination-type resonances for future work.

An example of a resonant TNO from the DES data is shown in the left column of Figure 3. Note the constant behavior of the semi-major axis in the top panel; the inset demonstrates the librating resonance argument corresponding to the 2:7 commensurability.

Scattering disk object (SDO)*. SDOs are objects that are currently scattering off of Neptune, and experience rapid and significant variations in their semi-major axis evolution as a result. Unlike the outer centaurs, the orbits of the scattering objects lie fully outside the giant planet region, and thus SDOs experience rather weak interactions with Neptune. Consistent with the Gladman et al. (2008) definition, we define a scattering object as one whose semi-major axis changes by more than a few AU with respect to its initial value, a_0, over the integration time (10 Myr for objects with $a < 100$ AU, and 100 Myr for objects with $a > 100$ AU). To ensure that this definition scales well as we consider longer period objects, our criterion for scattering is as follows:

$$\frac{\Delta a}{a} > 0.0375, \tag{3}$$

where

$$\frac{\Delta a}{a} = \frac{\max\left(a(t) - a_0\right)}{a_0} \tag{4}$$

is the maximum variation in semi-major axis over the integration time. The choice in the exact value of variation allowed before an object becomes scattering is somewhat arbitrary, but must be large enough that periodic variations of orbital elements do not falsely classify an object as scattering. Here we use the value of 0.0375, as it corresponds to the accepted change of 1.5 AU for a typical classical belt object at $a = 40$ AU (Gladman et al. 2008). Previous works have also used $\Delta a/a < 0.05$ (Volk & Malhotra 2017) and 1.5 AU (Morbidelli et al. 2004). An example of the dynamics of a scattering object from the DES set is shown in the left column of Figure 4. Note the significant change in the semi-major axis over the short 10 Myr integration time, as well as the proximity of the perihelion distance to Neptune's orbit at 30 AU.

Detached object. Detached TNOs are objects whose dynamics are decoupled from Neptune's influence. Generally, these are TNOs with large perihelion distances; following Gladman et al. (2008), we define non-scattering and non-resonant TNOs with eccentricities $e > 0.24$ to be detached. Most of these objects are found beyond the 1:2 resonance with Neptune ($a > 47.7$ AU). An example of a detached TNO is shown in the right column of Figure 4. Note the large perihelion distance and the resulting undisturbed semi-major axis evolution.

Classical belt object. The classical belt, then, is composed of non-scattering TNOs with eccentricities $e < 0.24$. An example of such an object is shown in the right column of Figure 3.

A visual representation of these dynamical regimes on the semi-major axis - eccentricity plane can be found in Figure 1. A companion plot that shows the DES TNOs in each class and a detailed discussion of these results is found in Section 3.

Given the definitions above, we begin by checking each object in our sample for resonant behavior. If non-resonant, we proceed to classify its dynamics into one of the remaining classes.

Although it may be possible to determine whether an object fits into one of the above categories just by considering its present day orbit, we cannot fully classify the objects without understanding their orbital evolution. The two categories that require this knowledge are the resonant and scattering classes; without running numerical simulations that model the outer Solar System, we cannot classify such objects.

Using the categories outlined above, we present our algorithm for TNO classification below.

1. From observations, determine the best-fit orbital elements and the associated covariance matrix for each object. In this work, we use the fitting algorithm from Bernstein & Khushalani (2000).

2. Generate ten clones of each TNO by drawing from a six-dimensional Gaussian distribution, where the best-fit orbit is the mean and the covariance matrix represents the uncertainties.

3. Run an N-body integration of the ten clones and the best-fit orbit. In order to properly compare classifications for different objects, it is best if the dynamical behavior is evaluated for approximately the same number of orbital periods. For this reason, we run 10 Myr integrations for objects with $a < 100$ AU and 100 Myr integrations for objects with $a > 100$ AU. The threshold of 100 AU is an

arbitrary choice, but the integrations must be extended for longer period objects as it takes more time to evaluate the dynamics. We use the N-body code `mercury6` with a hybrid symplectic and Bulirsch-Stoer (B-S) integrator and a time step of 20 days. In each integration, we include the TNO and its clones as test particles, as well as the four giant planets as active bodies (Jupiter, Saturn, Uranus, Neptune). We integrate the orbital elements for each TNO to a common epoch before beginning the simulations; in this work, time zero corresponds to the date May 4th, 2019.

4. Dynamically classify the objects based on the output of the simulations. The TNOs are grouped into the Jupiter-coupled object, inner centaur, outer centaur, Oort cloud, detached, and classical belt classes based on the current day best-fit orbit. The resonant and scattering classifications are based on the time-evolution of the ten clones. In particular, we consider TNOs with more than five clones that experience scattering behavior (as defined above) to be scattering objects. The resonant classification is more strict; only objects that are resonant for greater than 95% of the time, averaging over the ten clones, are considered to be resonant objects. Additional details regarding the resonance classification can be found in Section 3.1.

5. Check if there are objects with insecure classifications. Such TNOs generally have clones with orbits that are different enough to cause them to experience disparate dynamical evolution. For example, in our data, we found that a handful of TNOs would have a couple of scattering clones, but the rest of their clones would be detached. In this situation, we extend the integration time to 100 Myr to enable a more secure classification. If the classification remains insecure, we sort the object into a category as delineated in step 4, and leave the question of secure classification for future work, once higher precision orbits are acquired.

As can be seen from the dynamical class definitions above, it is straightforward to automatically separate the TNOs into the Jupiter-coupled object, inner centaur, outer centaur, Oort cloud, scattering, detached, and classical belt categories. The tricky step of the process is the resonance classification. To classify an object as resonant, it must not only be near an integer period ratio with Neptune, but we must identify a librating resonance angle. Often in the literature, this analysis is done by hand. Since the DES dataset contains hundreds of objects, this becomes significantly time intensive. In addition, since each period ratio has a large number of resonance arguments associated with it (i.e. for each p, q pair, there are many r, s pairs that satisfy $p+q+r+s=0$), it is difficult to conclude with certainty that an object is non-resonant.

In the following subsection, then, we describe the resonance identification algorithm we have developed to address these challenges. The main idea behind the algorithm lies in plotting the time evolution of many potential resonance arguments, and searching for regions of libration by identifying low point density regions in the plot. By applying this strategy, we are able to successfully identify a number of resonant objects, some of which are in rather high order resonances with Neptune.

2.1. *Resonance Identification*

In this subsection, we describe the resonance identification process. The input for this algorithm are the simulation results for the ten clones of the TNO; each clone is studied individually, as described below. A sample of this procedure is demonstrated in Figures 5 and 6.

1. Divide the total integration time into shorter time intervals. Since the algorithm is based on a point-density analysis, we have found that it is best if each interval contains ~ 5000 data points. In our 10 Myr integrations, this corresponds to 5 Myr intervals, and 50 Myr intervals in our 100 Myr integrations. This coarse subdivision allows us to identify regions of constant semi-major axis; as described below, we break these time intervals up further in later steps of the process.

2. Average over the semi-major axis evolution in each interval, and compute the corresponding averaged period ratio with Neptune, R_{av}.

3. If the average period ratios in neighboring intervals have similar values, connect the time intervals. In our analysis, we connect these intervals if the period ratios differ by less than 0.01. In the steps that follow, we will search for resonances in each of these connected intervals.

4. Recall that the resonance argument is of the form

$$\phi = p\lambda_N + q\lambda + r\varpi_N + s\varpi, \tag{5}$$

where p, q, r, and s are integers that satisfy $p+q+r+s=0$. For each interval, consider a range of

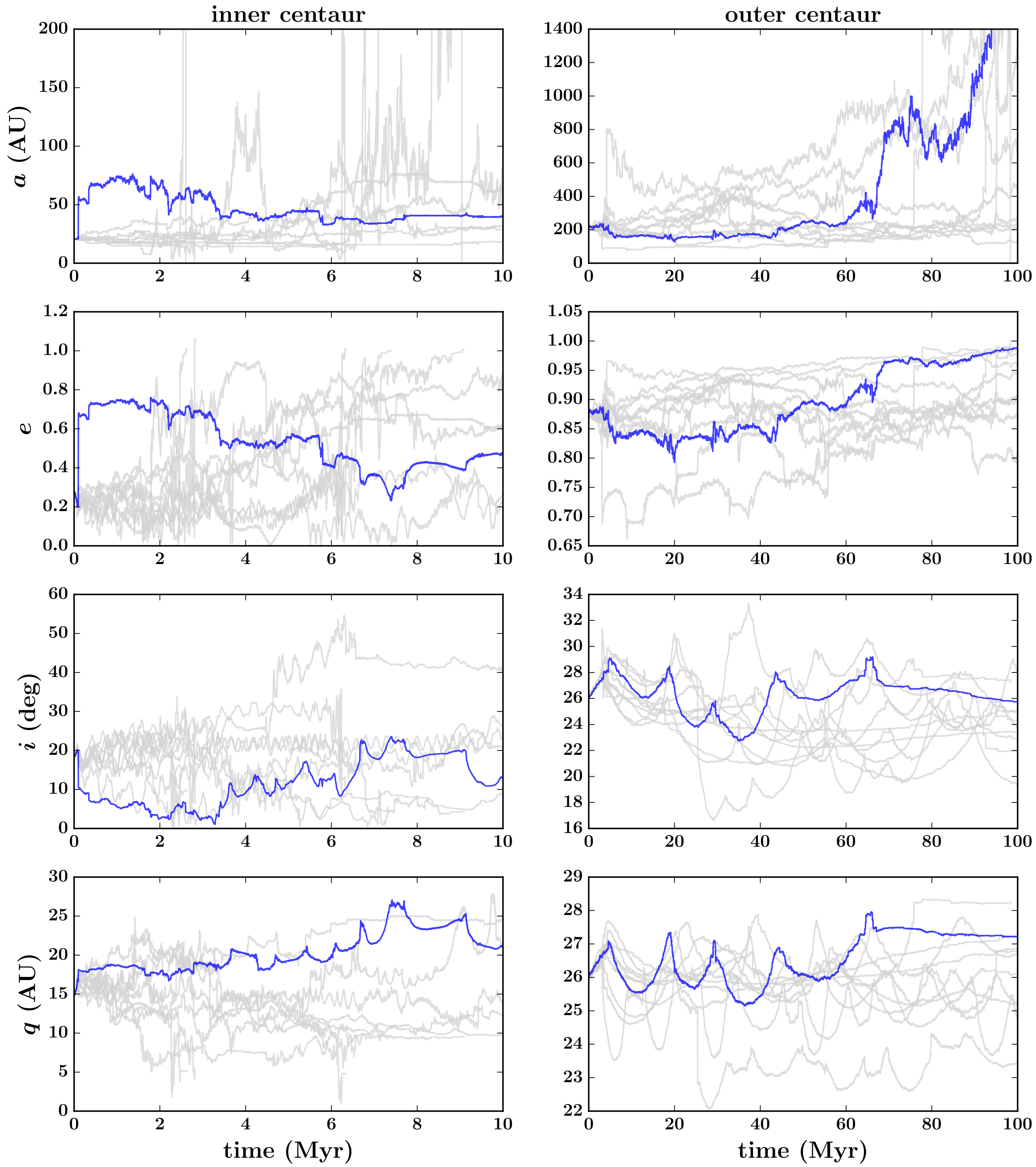

Figure 2. Example dynamics of an inner centaur (left column, object 2003 QC_{112}) and an outer centaur (right column, object `s11_good_19`) detected in the DES data. The panels show the time evolution of semi-major axis, eccentricity, inclination, and perihelion distance. The trajectories of the ten clones are shown in gray and the best fit trajectory is in blue. Note the short perihelion distance of the two centaurs.

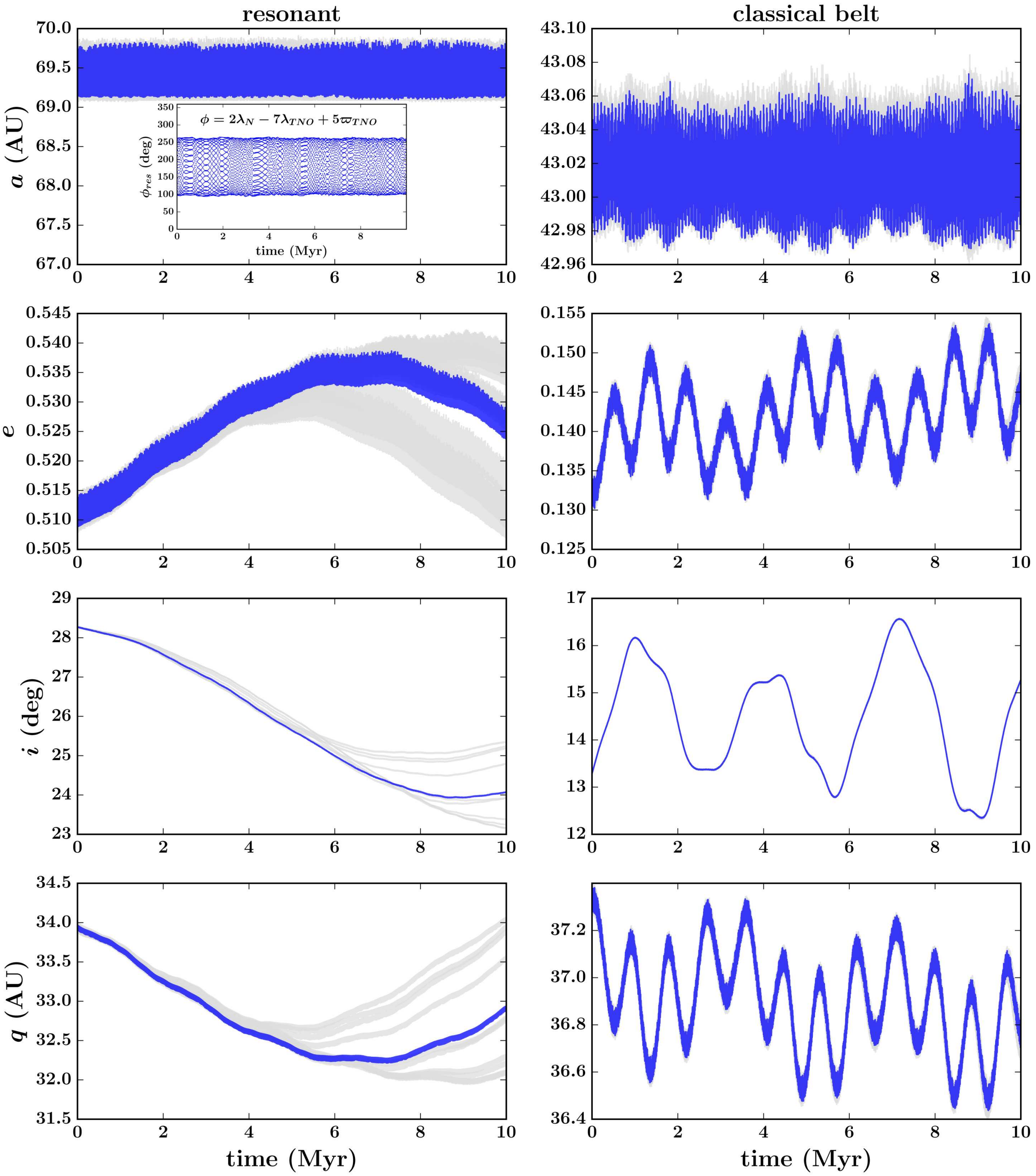

Figure 3. Example dynamics of a resonant object (left column, object `s12_good_5`) and a classical belt object (right column, object 2013 RP_{98}) detected in the DES data. The panels show the time evolution of semi-major axis, eccentricity, inclination, and perihelion distance. The trajectories of the ten clones are shown in gray and the best fit trajectory is in blue. The inset in the top left panel displays the time evolution of the resonant argument corresponding to the 2:7 resonance of the TNO; note that the behavior of this angle is bounded (librating), indicating that this TNO is in fact in resonance for the full integration time.

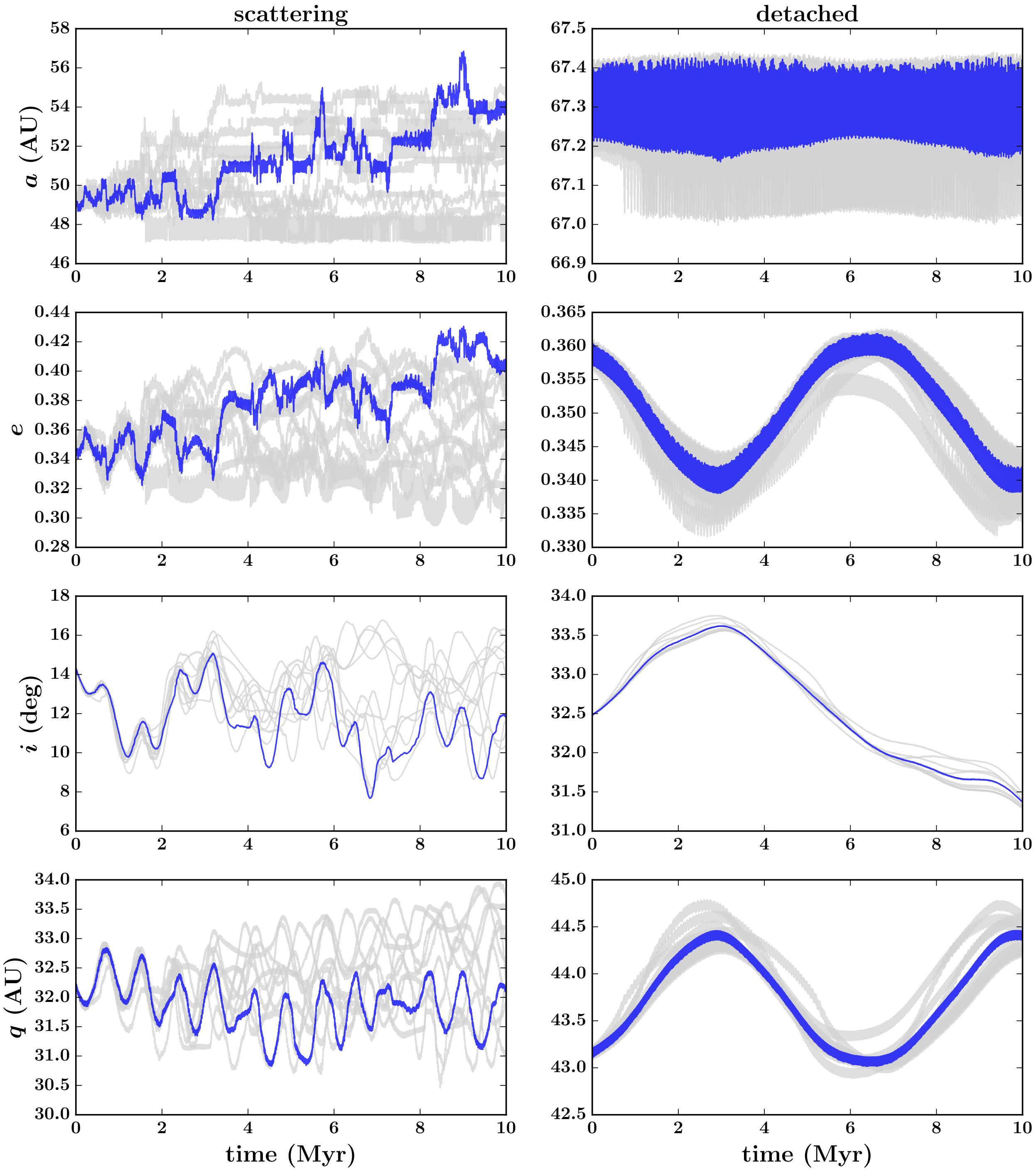

Figure 4. Example dynamics of a scattering object (left column, object 2012 WG_{37}) and a detached object (right column, object `s14_good_4`) detected in the DES data. The panels show the time evolution of semi-major axis, eccentricity, inclination, and perihelion distance. The trajectories of the ten clones are shown in gray and the best fit trajectory is in blue. Note the varying semi-major axis of the scattering object (left) and the contrasting constant a behavior of the detached object (right).

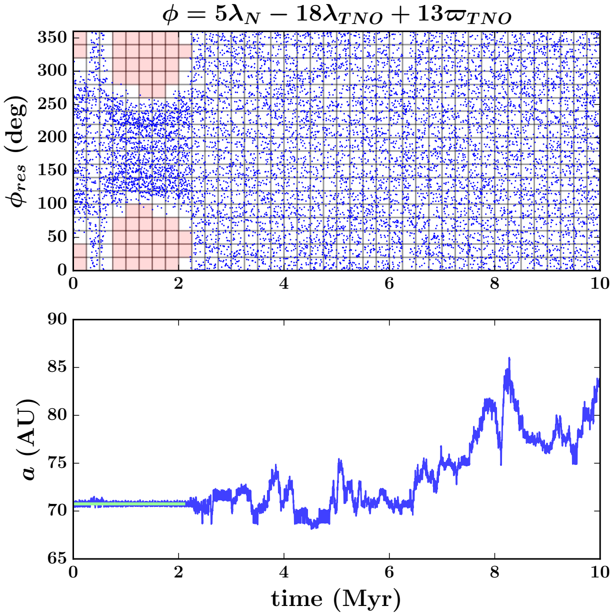

Figure 5. A demonstration of the automated resonance identification algorithm. The top panel shows the time-evolution of the resonance argument ϕ in small blue markers. The grid guides the search for low-point-density rectangles, which are shaded in light red. The bottom panel shows the corresponding semi-major axis evolution, with regions of constant a highlighted in green. Note that this figure demonstrates a likely non-resonant object; this particular clone only spends a small portion of the integration time in resonance.

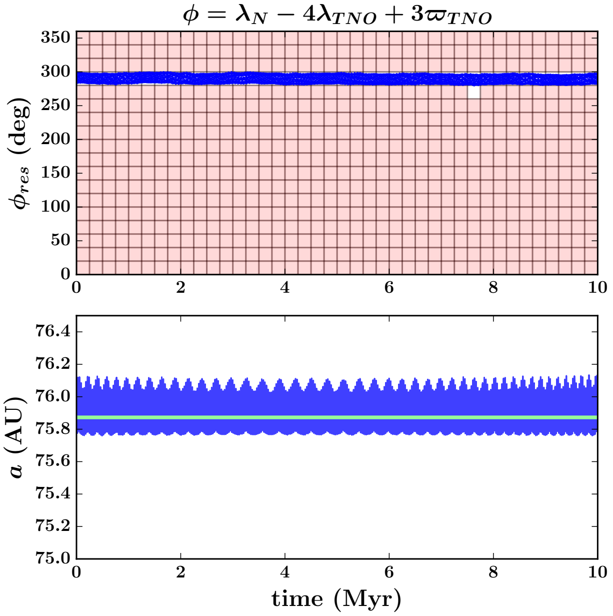

Figure 6. A demonstration of the automated resonance identification algorithm. The top panel shows the time-evolution of the resonance argument ϕ in small blue markers. The grid guides the search for low-point-density rectangles, which are shaded in light red. The bottom panel shows the corresponding semi-major axis evolution, with regions of constant a highlighted in green. In contrast to Figure 5, this clone is in resonance for the full integration time. The large number of shaded grid squares indicate the clearly bounded resonance angle evolution.

p:q resonances that span the period ratio range of (R_{av} - resonance width, R_{av} + resonance width). In our analysis, we use a resonance width value of 0.2, which corresponds to a range of about 7 AU at a semi-major axis of 39 AU. Note that this purposefully overestimates the resonant width to ensure that all possible resonances are considered; realistic calculations of the semi-major axis width for Neptune resonances can be found in Wang & Malhotra (2017); Lan & Malhotra (2019).

5. Identify the first p:q resonance within the period ratio range. Here, a decision needs to be made regarding the order of the resonances considered. In our analysis, we check all resonance arguments with $p, |q| \in [1, 26]$, and $r, s \in [-25, 24]$.

6. Fix the first pair of r and s coefficients.

7. Next, overlay a fine grid on the plot of ϕ vs. time over one time interval. We use a grid of 18 horizontal lines, as $\phi \in (0°, 360°)$, and 20 vertical lines for every 5000 points (see top panel of Figures 5-6).

8. Run over the grid, counting the number of points in each grid square. Flag grid squares with few points (for the parameters specified above, we flag squares with one or zero points). In Figure 5-6, flagged squares are shaded in light red. Next, impose additional restrictions on the grid to correctly identify resonances; we require that there must be at least two flagged squares per column, or at least two adjacent flagged squares per row, and require a total number of flagged squares to exceed a set threshold. These additional conditions help discard false positives, and can be adjusted depending on the data one is working with.

9. Repeat steps 6-8 for each pair of r, s coefficients which satisfy the resonance relationship for the chosen p:q resonance. Once all r, s pairs have been cycled through, identify the best r, s pair by choosing the one with the largest number of flagged grid squares.

10. Repeat steps 5-9 for the entire set of p:q pairs.

11. Repeat steps 1-10 for each clone of the TNO. Compute the fraction of time spent in resonance by each clone, and average over all clones to find the resonance percentage for the TNO.

In this process, then, we parse the simulation data on a variety of timescales. First, we identify the regions of constant semi-major axis on long time intervals, and then check the resonance argument libration precisely on a fine subdivided grid. To achieve the best results, the exact length of these intervals should scale with the orbital period of the object one is studying.

After applying this algorithm, a decision needs to be made regarding the percentage threshold at which a TNO is considered to be truly *resonant*. In our analysis, we define objects that are resonant for greater than 95% of the time to be resonant, and objects that are resonant for greater than 50% of the time to be resonant candidates. The application of this procedure to the current DES TNO sample and the analysis of the results is described in the following section.

3. CLASSIFICATION OF DES TNOS

We apply the algorithm described in Section 2 to the currently available dataset of DES TNOs. The sample does not contain any Jupiter-coupled objects or Oort cloud objects, but all other dynamical classes are represented. We find 1 inner centaur, 19 outer centaurs, 21 scattering disk objects, 47 detached TNOs, 48 securely resonant objects, 7 resonant candidates, and 97 classical belt objects. The classifications for specific objects and their barycentric orbital elements are reported in **??**.

A visual summary of these results is shown in the bar plot in Figure 7. The classical belt population dominates the dataset, but there is a significant number of detached and resonant TNOs as well. The resonant bar consists of two parts; the blue represents the securely resonant objects, while the purple shows the resonant candidates.

This data is further visualized on the semi-major axis-eccentricity plane in Figure 8. The black solid curves correspond to constant perihelion distances, with $q = 7.35$ AU and $q = 30$ AU, from top to bottom. A companion plot that presents the regions of each dynamical class can be found in Figure 1; the colors of the regions correspond to the marker colors in Figure 8.

In Figure 8, the current day best-fit (a, e) of each TNO is plotted with a colored marker that corresponds to its dynamical class. The inner centaurs, in red, are found in the giant planet region, with semi-major axes below $a_N = 30$ AU, and the outer centaurs, in purple, cross Neptune's orbit, with $q < 30$ AU and $a > 30$ AU. Most of the other objects are found near the $q = 30$ AU curve, as it is easier to observe short perihelion TNOs. There are a few exceptions; most notably, a detached TNO in blue with $a = 105$ AU and $q = 50$ AU (`s17_good_0`).

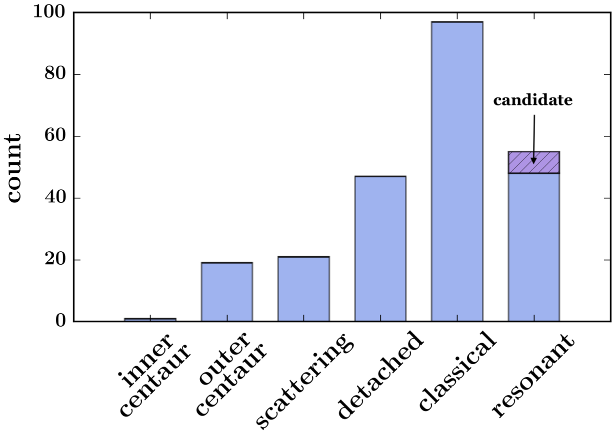

Figure 7. A summary plot of the dynamical classification of the DES TNOs, showing the relative abundance of each category out of the 240 total classified objects. Most of the objects detected in the data are members of the classical belt, but there are number of both detached and securely resonant objects as well. Resonant objects that could not be securely identified are marked as candidates.

The population of objects denoted with green markers at low eccentricity constitute the classical belt. These TNOs are dynamically cold (undergo only minimal orbital evolution) as they do not experience strong interactions with Neptune. Their perihelion detachment is evident in the inset plot, which zooms in on the $a \in [30, 60]$, $e \in [0, 0.5]$ region, and demonstrates that the classical belt TNOs have $q > 30$ AU (the solid black curve). In fact, most of these objects have $q = 35 - 37$ AU, as shown in Petit et al. (2011).

Similar to the classical belt population, the detached objects (blue markers) do not interact with Neptune and remain separated from the $q = 30$ AU curve. Defined to be as objects with higher eccentricities, the blue markers are found above the green ones.

The scattering disk objects, marked in yellow, can be found near the $q = 30$ AU curve. These are TNOs with Neptune-driven dynamics, which result in their movement along the $q = 30$ AU curve. The perihelion distance threshold at which objects cease to be affected strongly by Neptune perturbations is often cited to be around $q \approx 35 - 37$ AU (Jewitt 1999; Lykawka & Mukai 2007); however, this boundary is actually dependent on semi-major axis (Duncan et al. 1987). Since a TNO's orbital energy scales as $1/a$, at a fixed perihelion distance, larger semi-major axis objects are more strongly affected by energy kicks from Neptune and thus experience greater orbital evolution.

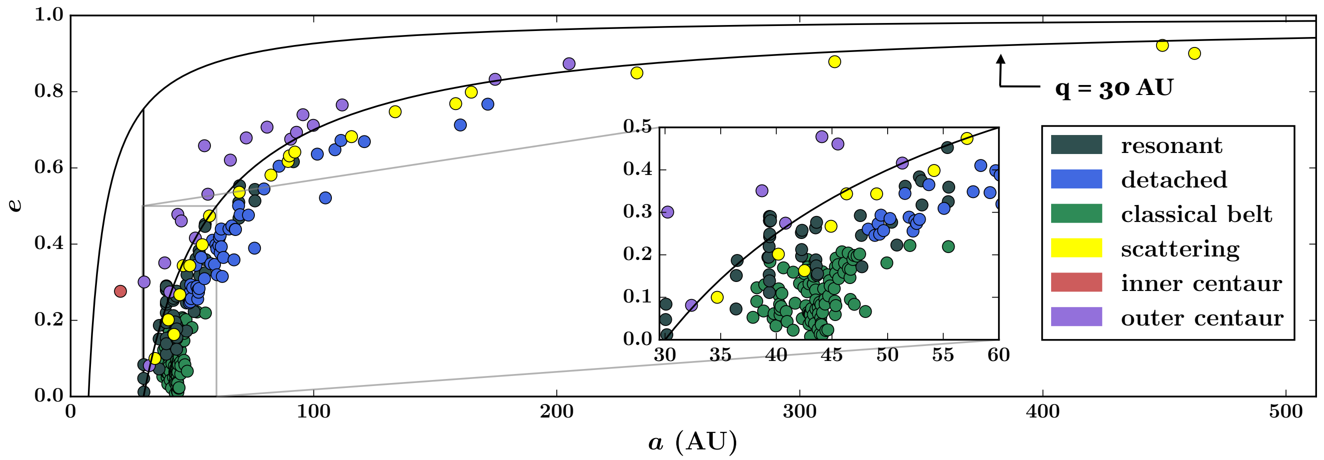

Figure 8. The DES TNOs on the semi-major axis-eccentricity plane, with colored markers indicating the different dynamical classes into which objects have been classified. The black solid curves correspond to constant perihelion distances, with $q = 7.35$ AU and $q = 30$ AU (top to bottom); detections are biased towards objects whose current distances are closer, leading the envelope of the largest density of discovered objects to have a rough outer limit at around $q = 35 - 36$ AU. A companion plot that denotes the approximate region of each dynamical class is found in Figure 1. The inset zooms in on the $a \in [30, 60]$ AU, $e \in [0, 0.5]$ region of the outer Solar System. The orbital elements of the objects are plotted at the epoch reported in Table **??**.

In the inset, it is possible to note objects marked with dark gray markers; these are the resonant and resonant candidate objects. These TNOs can be found in any region of the phase space, as their location is determined by their semi-major axis alone. For example, in the inset, it is easy to spot the three DES Neptune trojans at the 1:1 resonance at $a = 30$ AU. A more detailed discussion of the resonant TNOs and a plot of the corresponding $a - e$ plane (Figure 10) are presented in the following section.

3.1. *Resonant Population*

The current DES TNO sample contains 48 resonant objects, with an additional 7 resonant candidates, as shown in Figure 9. In this plot, we present the results of our resonance classification algorithm for the entire DES sample. The histogram displays the percentage of time spent in resonance by each TNO.

To compute this value, we first find the fraction of time each of the ten clones spends in a resonance during the integration time. Sometimes, a clone may visit more than one resonance during the integration; in this case, we take the longest time spent in one resonance. Next, we average over all of the ten clones, and arrive at the percentage of time spent in resonance by each TNO.

The result is shown in the histogram in Figure 9. Note that there are two peaks of objects - non-resonant TNOs, with 0% of time spent in resonance, and securely resonant TNOs, with greater than 95% of time spent in resonance. There are relatively few TNOs in the middle region. This seems to indicate that our resonance-finding algorithm is able to clearly distinguish between the resonant and non-resonant cases, and does not present a large number of semi-resonant objects.

In reality, objects could indeed be semi-resonant: over long time scales, objects may transition in and out of resonance. The integration times under consideration here, however, are short, and we expect objects to either be resonant or not on these timescales.

In this work, we choose to identify TNOs that are resonant greater than 50% of the time, but less than 95% of the time, as resonant candidates. The location of the two thresholds is rather arbitrary, but Figure 9 clearly shows that any reasonable choice will produce quantitatively similar results. The candidate resonant TNOs spend the majority of their time in resonance; as their orbits improve with further observations, it is possible that these TNOs will become securely resonant TNOs.

The DES resonant TNOs populate 15 resonances, ranging from the short period Neptune trojans at the 1:1 resonance to the long period 3:16 TNO candidate. A bar plot of the populated resonances is shown in the bottom panel of Figure 10. The bottom left panel presents all instances of each $p{:}q$ resonance, sorted by increasing orbital period, from left to right. The blue bars represent the securely resonant objects, and the hatched purple bars show the much smaller population of resonant candidates. The bar plot in the bottom right panel summarizes this data.

The top panel displays the resonant objects on the $a-e$ plane. Note that each resonance is found at a constant

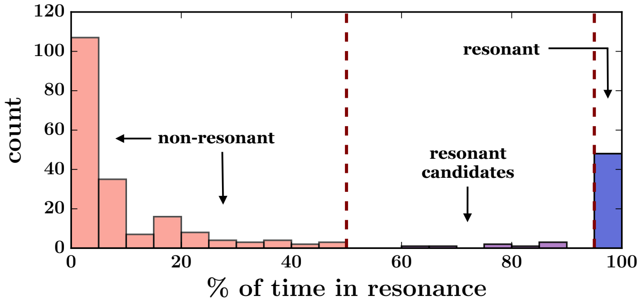

Figure 9. A histogram of the percent of time spent in resonance for all of the known DES TNOs. For each object, we compute the percent of time each of its clones spends in resonance and average over all ten clones to find the total resonance percentage. Most objects are securely non-resonant (the 0% bin). In between the two dashed vertical lines are a few resonant candidates (50% to 95%), and to the right of the line at 95% are the resonant objects: those with clones that are in resonance for the full integration time.

semi-major axis as indicated by the dashed vertical lines; as a result, each resonance is reminiscent of beads on a string. Each of these resonances corresponds directly to a bar in the bottom left panel. For example, note the three Neptune trojans on the left in both plots, next the three objects in the 3:4 resonance, and so on.

From this analysis, we see that the resonant TNOs make up a significant portion of the DES dataset, representing about one fifth of the objects. The most populated resonances are the Plutinos, at the 2:3 resonance, but there are a number of higher order resonances in the sample as well.

4. DISCUSSION

In this work, we introduce an updated classification algorithm for the trans-Neptunian region of the Solar System. Our classification scheme is fundamentally consistent with the previous classification schemes laid out in Elliot et al. (2005) and Gladman et al. (2008). Similarly to Elliot et al. (2005), which used detections from the Deep Ecliptic Survey, we classify a uniformly derived sample of Kuiper Belt objects: all objects were detected so far in the Dark Energy Survey data, many of which are previously undiscovered objects.

Our new resonance-finding tool allows for the automated identification of resonances by using numerical integrations of TNOs, and uses an hierarchical determination of regions where resonance angles librate to identify KBOs in true resonance. Through this method, we classify the current collection of objects detected by the Dark Energy Survey and present a summary of the results. Our classification scheme yields 1 inner centaur, 19 outer centaurs, 21 scattering disk objects, 47 detached TNOs, 48 securely resonant objects, 7 resonant candidates, and 97 classical belt objects.

It is important to note that our classification algorithm is only as good as the certainty of the TNO orbits. Although a poorly constrained orbit can result in a mis-classification in any of the categories, the most sensitive boundary is that for the resonant classification. If the semi-major axis error for a TNO is several AU or more – greater than a typical resonance width – then the spread in the initial orbit of the clones will result in overall non-resonant behavior for the TNO. In this situation, the object may be classified as scattering or as a classical belt/detached TNO, depending on its perihelion distance. In reality, however, the TNO could actually be in a resonance, but the wide range of possible semi-major axes a (due to large uncertainties) prevents us from making a secure classification.

On the other hand, classifying an object as a securely resonant TNO is an indication that it has a well-defined orbit with small errors, and further observations of the object are unlikely to change the classification. That is, general improvement of the orbit certainties for the TNOs could potentially increase the number of objects in the resonance class, and decrease the number of objects in the other classes.

We expect the coming years to witness a substantial increase in the numbers of TNOs detected by DES as the remaining data is analyzed (e.g., Bernardinelli et al. 2019). Once the additional objects are classified and combined with the current dataset, we plan to conduct a suite of population-wide analyses of the TNOs. In combination with the DES survey simulator, such future work will reveal the structure of this distant region and allow for the testing of formation hypotheses of the outer Solar System.

This material is based upon work supported by the National Aeronautics and Space Administration under Grant No. NNX17AF21G issued through the SSO Planetary Astronomy Program. J.C.B, L.M., and S.J.H are supported by the NSF Graduate Research Fellowship Grant No. DGE 1256260.

This work included the observations obtained at the MDM Observatory, operated by Dartmouth College, Columbia University, Ohio State University, Ohio University, and the University of Michigan.

Funding for the DES Projects has been provided by the U.S. Department of Energy, the U.S. National Science Foundation, the Ministry of Science and Education of Spain, the Science and Technology Facilities Council of the United Kingdom, the Higher Education Funding Council for England, the National Center for Su-

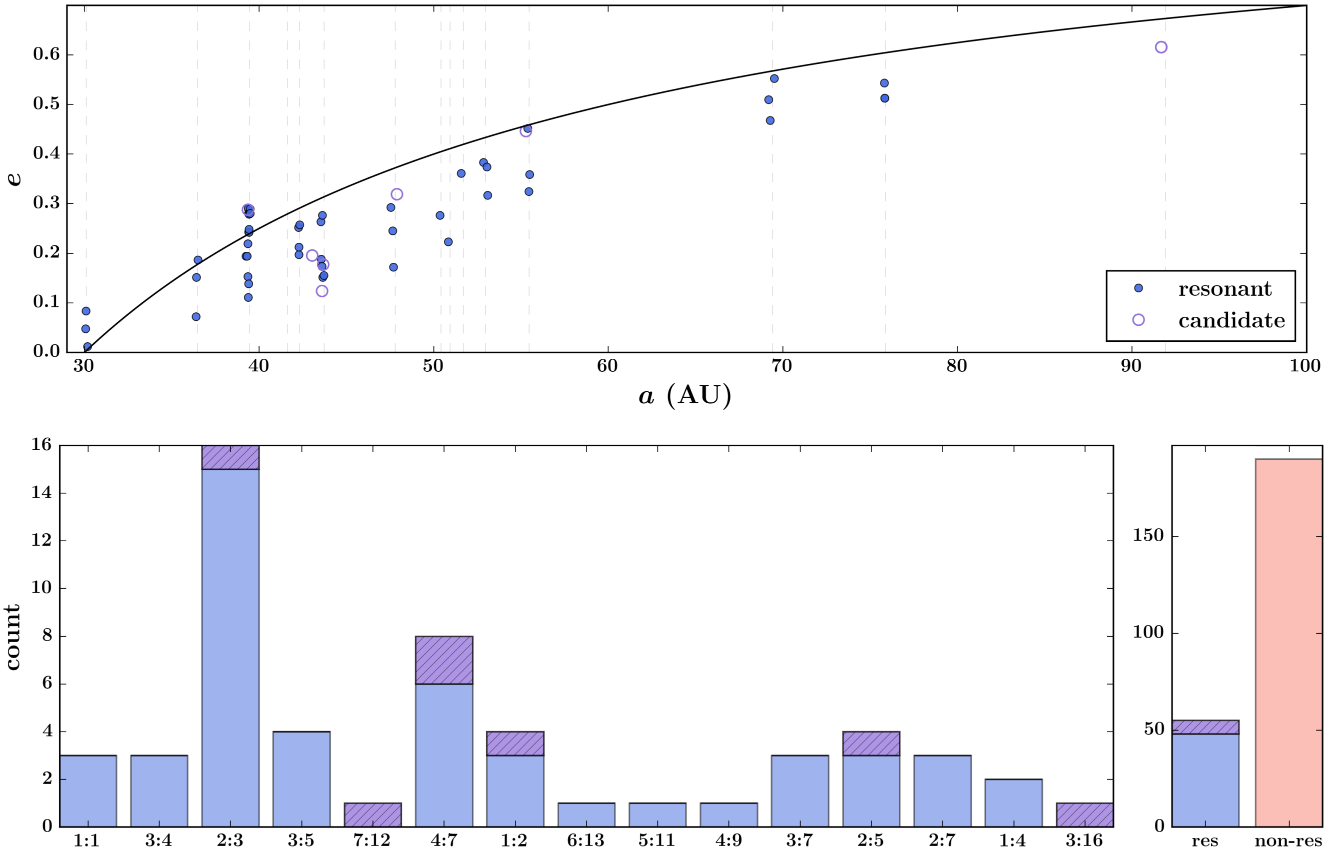

Figure 10. The top panel visualizes the resonant TNOs on the $a-e$ plane, while the bottom left panel presents the distribution of resonances for the resonant TNOs. All of the resonant objects are in resonance with Neptune. The most populated resonance is the 2:3 (the Plutinos), and there are a number of higher order resonances, such as the 2:7 or the 6:13. The bottom right panel shows the number of resonant objects as compared to the number of non-resonant TNOs in the DES data. The blue bars represent securely resonant objects, while the purple bars are the resonant candidates. The bottom left bar plot sorts the resonances by period; this allows for easy comparison between the bottom and top panels. For instance, the left three objects in both plots are the three Neptune trojans, and the rightmost TNO in both plots is a 3:16 resonant candidate. The orbital elements of the objects are plotted at the epoch reported in Table **??**.

percomputing Applications at the University of Illinois at Urbana-Champaign, the Kavli Institute of Cosmological Physics at the University of Chicago, the Center for Cosmology and Astro-Particle Physics at the Ohio State University, the Mitchell Institute for Fundamental Physics and Astronomy at Texas A&M University, Financiadora de Estudos e Projetos, Fundação Carlos Chagas Filho de Amparo à Pesquisa do Estado do Rio de Janeiro, Conselho Nacional de Desenvolvimento Científico e Tecnológico and the Ministério da Ciência, Tecnologia e Inovação, the Deutsche Forschungsgemeinschaft and the Collaborating Institutions in the Dark Energy Survey.

The Collaborating Institutions are Argonne National Laboratory, the University of California at Santa Cruz, the University of Cambridge, Centro de Investigaciones Energéticas, Medioambientales y Tecnológicas-Madrid, the University of Chicago, University College London, the DES-Brazil Consortium, the University of Edinburgh, the Eidgenössische Technische Hochschule (ETH) Zürich, Fermi National Accelerator Laboratory, the University of Illinois at Urbana-Champaign, the Institut de Ciències de l'Espai (IEEC/CSIC), the Institut de Física d'Altes Energies, Lawrence Berkeley National Laboratory, the Ludwig-Maximilians Universität München and the associated Excellence Cluster Universe, the University of Michigan, the National Optical Astronomy Observatory, the University of Nottingham, The Ohio State University, the University of Pennsylvania, the University of Portsmouth, SLAC National Accelerator Laboratory, Stanford University, the University of Sussex, Texas A&M University, and the OzDES Membership Consortium.

Based in part on observations at Cerro Tololo Inter-American Observatory, National Optical Astronomy Observatory, which is operated by the Association of Universities for Research in Astronomy (AURA) under a cooperative agreement with the National Science Foundation.

The DES data management system is supported by the National Science Foundation under Grant Numbers AST-1138766 and AST-1536171. The DES participants from Spanish institutions are partially supported by MINECO under grants AYA2015-71825, ESP2015-66861, FPA2015-68048, SEV-2016-0588, SEV-2016-0597, and MDM-2015-0509, some of which include ERDF funds from the European Union. IFAE is partially funded by the CERCA program of the Generalitat de Catalunya. Research leading to these results has received funding from the European Research Council under the European Union's Seventh Framework Program (FP7/2007-2013) including ERC grant agreements 240672, 291329, and 306478. We acknowledge support from the Brazilian Instituto Nacional de Ciência e Tecnologia (INCT) e-Universe (CNPq grant 465376/2014-2).

This manuscript has been authored by Fermi Research Alliance, LLC under Contract No. DE-AC02-07CH11359 with the U.S. Department of Energy, Office of Science, Office of High Energy Physics. The United States Government retains and the publisher, by accepting the article for publication, acknowledges that the United States Government retains a non-exclusive, paid-up, irrevocable, world-wide license to publish or reproduce the published form of this manuscript, or allow others to do so, for United States Government purposes.

REFERENCES

Adams, E. R., Gulbis, A. A. S., Elliot, J. L., et al. 2014, AJ, 148, 55

Bannister, M. T., Gladman, B. J., Kavelaars, J. J., et al. 2018, ApJS, 236, 18

Batygin, K., Brown, M. E., & Betts, H. 2012, ApJ, 744, L3

Becker, J. C., Khain, T., Hamilton, S. J., et al. 2018, AJ, 156, 81

Bernardinelli, P. H., Bernstein, G. M., Sako, M., et al. 2019, arXiv e-prints, arXiv:1909.01478

Bernstein, G., & Khushalani, B. 2000, AJ, 120, 3323

Bernstein, J. P., Kessler, R., Kuhlmann, S., et al. 2012, ApJ, 753, 152

Chen, Y.-T., Lin, H. W., Holman, M. J., et al. 2016, ApJ, 827, L24

Dark Energy Survey Collaboration, Abbott, T., Abdalla, F. B., et al. 2016, MNRAS, 460, 1270

Duncan, M., Quinn, T., & Tremaine, S. 1987, AJ, 94, 1330

Elliot, J. L., Kern, S. D., Clancy, K. B., et al. 2005, AJ, 129, 1117

Flaugher, B., Diehl, H. T., Honscheid, K., et al. 2015, AJ, 150, 150

Gerdes, D. W., Jennings, R. J., Bernstein, G. M., et al. 2016, AJ, 151, 39

Gerdes, D. W., Sako, M., Hamilton, S., et al. 2017, ApJ, 839, L15

Gladman, B., Marsden, B. G., & Vanlaerhoven, C. 2008, Nomenclature in the Outer Solar System, ed. M. A. Barucci, H. Boehnhardt, D. P. Cruikshank, A. Morbidelli, & R. Dotson, 43–57

Gladman, B., Kavelaars, J., Petit, J. M., et al. 2009, ApJ, 697, L91

Hamilton, S. J., & DES Collaboration. 2019, in prep

Horner, J., Evans, N. W., & Bailey, M. E. 2004, MNRAS, 354, 798

Jewitt, D. 1999, Annual Review of Earth and Planetary Sciences, 27, 287. https://doi.org/10.1146/annurev.earth.27.1.287

Khain, T., Becker, J. C., Adams, F. C., et al. 2018, AJ, 156, 273

Kowal, C. T., Liller, W., & Marsden, B. G. 1979, in IAU Symposium, Vol. 81, Dynamics of the Solar System, ed. R. L. Duncombe, 245

Lan, L., & Malhotra, R. 2019, arXiv e-prints, arXiv:1901.06040

Lawler, S. M., Kavelaars, J. J., Alexandersen, M., et al. 2018, Frontiers in Astronomy and Space Sciences, 5, 14

Lin, W., Gerdes, D. W., Hamilton, S. J., et al. 2019, Icarus, 321, 426

Lykawka, P. S., & Mukai, T. 2007, Icarus, 189, 213

Morbidelli, A., Emel'yanenko, V. V., & Levison, H. F. 2004, MNRAS, 355, 935

Nesvorný, D. 2011, ApJ, 742, L22

Petit, J.-M., Kavelaars, J. J., Gladman, B. J., et al. 2011, AJ, 142, 131

Schwamb, M. E., Brown, M. E., Rabinowitz, D. L., & Ragozzine, D. 2010, ApJ, 720, 1691

Tiscareno, M. S., & Malhotra, R. 2003, AJ, 126, 3122

Trujillo, C. A., Jewitt, D. C., & Luu, J. X. 2001, AJ, 122, 457

Tsiganis, K., Gomes, R., Morbidelli, A., & Levison, H. F. 2005, Nature, 435, 459

Volk, K., & Malhotra, R. 2017, AJ, 154, 62

Volk, K., Murray-Clay, R., Gladman, B., et al. 2016, AJ, 152, 23

Volk, K., Murray-Clay, R. A., Gladman, B. J., et al. 2018, AJ, 155, 260

Wang, X., & Malhotra, R. 2017, AJ, 154, 20

_data

Table 1. Barycentric orbital elements for the set of TNOs detected by DES and considered in this work. Some data is obtained from follow up observations, which improves the classification. Numbers are reported to representative errors. 'Res' denotes the specific resonance in which an object lives, if applicable. Solutions are reported at the epoch given in the final column of the table. Objects are ordered by current semi-major axis (in AU) and identified by the MPC identifier (if available) or by their DES internal identifier if an MPC designation does not exist. Angles (i, ω, Ω, M) are given in degrees.

TNO ID	**Class**	**Res.**	a_b **(AU)**	e_b	i_b **(deg)**	ω_b **(deg)**	Ω_b **(deg)**	M_b **(deg)**	**Epoch (JD)**
2003 QC112	inner centaur	-	20.5004 ± 0.0009	$0.27616 \pm 3 \times 10^{-5}$	18.245 ± 0.0001	22.194 ± 0.009	158.6556 ± 0.0003	191.708 ± 0.009	2456578.73
2014 UU240	resonant	1:1	30.056 ± 0.001	0.048 ± 0.003	35.747 ± 0.004	74 ± 3	81.993 ± 0.004	236 ± 3	2456959.83
2013 VX30	resonant	1:1	30.0871 ± 0.0006	$0.08374 \pm 2 \times 10^{-5}$	$31.25873 \pm 7 \times 10^{-5}$	215.49 ± 0.02	$192.53852 \pm 8 \times 10^{-5}$	347.84 ± 0.02	2456567.79
(530664) 2011 SO277	resonant	1:1	30.1614 ± 0.0005	$0.01185 \pm 8 \times 10^{-5}$	9.6386 ± 0.0002	117.7 ± 0.3	113.5271 ± 0.0009	148.1 ± 0.5	2456545.88
(309239) 2007 RW10	outer centaur	-	30.236 ± 0.002	$0.30055 \pm 6 \times 10^{-5}$	36.1011 ± 0.0001	96.095 ± 0.005	$187.03731 \pm 7 \times 10^{-5}$	61.472 ± 0.005	2456547.85
2013 RD109	outer centaur	-	32.378 ± 0.001	$0.08106 \pm 2 \times 10^{-5}$	11.1194 ± 0.0001	332.64 ± 0.05	16.6919 ± 0.0001	11.31 ± 0.05	2456537.77
2014 UC225	scattering	-	$34.7^{+0.4}_{-0.1}$	0.1 ± 0.04	4.942 ± 0.02	221 ± 100	139.7 ± 0.2	17 ± 90	2456951.73
2013 RH109	resonant	3:4	36.38 ± 0.005	0.0725 ± 0.0002	14.8214 ± 0.0003	288.5 ± 0.3	204.394 ± 0.001	196.8 ± 0.3	2456543.59
2013 RQ109	resonant	3:4	36.404 ± 0.003	$0.1512 \pm 6 \times 10^{-5}$	14.5378 ± 0.0001	335.91 ± 0.03	70.5182 ± 0.0006	339.72 ± 0.02	2456547.89
2014 TM95	resonant	3:4	36.487 ± 0.002	$0.18664 \pm 6 \times 10^{-5}$	17.5579 ± 0.0001	263.3 ± 0.01	161.1436 ± 0.0004	328.744 ± 0.008	2456569.69
2013 SH102	classical belt	-	37.902 ± 0.003	0.0528 ± 0.0002	19.3819 ± 0.0003	83.07 ± 0.07	$180.22736 \pm 2 \times 10^{-5}$	93.4 ± 0.1	2456565.66
2013 RG109	classical belt	-	38.241 ± 0.003	0.0904 ± 0.0002	22.7219 ± 0.0002	59.72 ± 0.04	22.6841 ± 0.0001	298.16 ± 0.02	2456537.86
2014 RH70	classical belt	-	38.251 ± 0.008	0.1224 ± 0.0002	$27.60542 \pm 5 \times 10^{-5}$	244.72 ± 0.06	8.0072 ± 0.0004	39.53 ± 0.04	2456904.6
s200_good_333	outer centaur	-	38.71 ± 0.01	0.3508 ± 0.0008	17.2877 ± 0.0006	35.9 ± 0.1	183.4814 ± 0.0002	100.2 ± 0.1	2456543.67
(120348) 2004 TY364	classical belt	-	38.86 ± 0.02	0.068 ± 0.004	24.838 ± 0.001	358 ± 0.6	140.5 ± 0.006	265.8 ± 0.7	2456904.85
s13_good_5	classical belt	-	39 ± 0.1	0.13 ± 0.02	38.39 ± 0.01	300 ± 6	169.46 ± 0.007	310 ± 3	2456958.85
2003 QB91	resonant	2:3	39.241 ± 0.002	0.1942 ± 0.0002	6.4955 ± 0.0002	80.6 ± 0.07	136.788 ± 0.003	142.4 ± 0.07	2456578.71
(534315) 2014 SK349	resonant candidate	2:3	39.3 ± 0.2	0.288 ± 0.003	9.41 ± 0.03	313 ± 4	59.8 ± 0.1	6 ± 2	2456932.79
2014 WC536	resonant	2:3	39.32 ± 0.03	0.194 ± 0.002	22.435 ± 0.002	259.8 ± 0.7	88.493 ± 0.004	34.2 ± 0.4	2456328.59
2013 SO102	resonant	2:3	39.353 ± 0.002	$0.21965 \pm 4 \times 10^{-5}$	9.8516 ± 9.00E-05	257.86 ± 0.02	145.2264 ± 0.0008	346.88 ± 0.01	2456564.83
2013 SP102	resonant	2:3	39.357 ± 0.001	$0.15307 \pm 8 \times 10^{-5}$	11.5999 ± 0.0002	75.65 ± 0.08	146.688 ± 0.001	158.75 ± 0.08	2456564.84
(469372) 2001 QF298	resonant	2:3	39.377 ± 0.002	0.11115 ± 9.00E-05	22.3519 ± 0.0003	42.2 ± 0.1	$164.18428 \pm 4 \times 10^{-5}$	149.8 ± 0.1	2456537.84

Table 1. continued from previous page

TNO ID	**Class**	**Res.**	a_b **(AU)**	e_b	i_b **(deg)**	ω_b **(deg)**	Ω_b **(deg)**	M_b **(deg)**	**Epoch (JD)**
2012 WF37	resonant	2:3	39.38 ± 0.003	0.29036 ± 4 × 10^{-5}	19.01377 ± 8 × 10^{-5}	275.142 ± 0.009	173.6208 ± 0.0002	328.669 ± 0.004	2456247.62
s302_good_485	resonant	2:3	39.384 ± 0.003	0.28046 ± 6 × 10^{-5}	10.36557 ± 4 × 10^{-5}	285.48 ± 0.01	129.4896 ± 0.0009	342.594 ± 0.007	2456569.7
s302_good_198	resonant	2:3	39.385 ± 0.003	0.28046 ± 6 × 10^{-5}	10.36557 ± 4 × 10^{-5}	285.48 ± 0.01	129.4897 ± 0.0009	342.594 ± 0.007	2456569.7
2012 TD324	resonant	2:3	39.39 ± 0.002	0.1386 ± 0.0001	9.57606 ± 8 × 10^{-5}	191 ± 0.05	114.616 ± 0.001	49.44 ± 0.03	2456544.82
2013 TY171	resonant	2:3	39.402 ± 0.002	0.24306 ± 9.00E-05	24.9545 ± 0.0002	247.63 ± 0.01	58.8074 ± 0.0003	47.476 ± 0.003	2456569.72
(504555) 2008 SO266	resonant	2:3	39.407 ± 0.002	0.24255 ± 6 × 10^{-5}	18.7979 ± 0.0001	172.76 ± 0.01	158.7544 ± 0.0004	34.401 ± 0.005	2456569.77
2014 WD536	resonant	2:3	39.408 ± 0.003	0.24871 ± 7 × 10^{-5}	16.6069 ± 0.0001	329.35 ± 0.03	68.2738 ± 0.0005	346.26 ± 0.02	2456545.8
2013 RC109	resonant	2:3	39.419 ± 0.003	0.2791 ± 0.0001	43.5138 ± 0.0004	318.85 ± 0.04	32.8166 ± 0.0002	14.01 ± 0.02	2456544.84
2013 TA172	classical belt	-	39.424 ± 0.004	0.18365 ± 9.00E-05	14.5476 ± 0.0002	237.4 ± 0.02	173.6434 ± 0.0002	329.27 ± 0.01	2456578.64
(534315) 2014 SK349	resonant	2:3	39.471 ± 0.002	0.2897 ± 0.0001	9.395 ± 0.0004	315.9 ± 0.3	59.898 ± 0.002	3 ± 0.2	2456569.69
2010 SB41	resonant	2:3	39.48 ± 0.002	0.28028 ± 4 × 10^{-5}	5.22363 ± 7 × 10^{-5}	248.8 ± 0.02	139.566 ± 0.001	352.74 ± 0.01	2456537.86
s121_good_1	classical belt	-	$39.7^{+0.2}_{-0.1}$	0.05 ± 0.004	54.78 ± 0.06	256 ± 40	206.506 ± -0.009	359 ± -300	2457014.83
2014 XZ40	classical belt	-	$39.794^{+0.007}_{-0.005}$	0.061 ± 0.003	44.56 ± 0.02	257 ± 5	146.807 ± 0.008	28 ± 5	2456992.8
(505412) 2013 QO95	classical belt	-	39.9679 ± 0.0003	0.03267 ± 10^{-5}	20.6027 ± 0.0003	316.1 ± 0.2	83.1093 ± 0.0007	349.5 ± 0.1	2456534.7
2013 RL109	scattering	-	40.185 ± 0.007	0.2015 ± 0.0003	14.1841 ± 0.0002	69.56 ± 0.02	193.5998 ± 0.0006	51.46 ± 0.01	2456545.56
2013 RB109	classical belt	-	40.208 ± 0.002	0.1081 ± 0.0001	23.1512 ± 0.0002	223.94 ± 0.08	175.85643 ± 3 × 10^{-5}	329.3 ± 0.06	2456537.77
s301a_good_186	classical belt	-	$40.21^{+0.01}_{-0.007}$	0.12 ± 0.01	1.7616 ± 0.0003	110 ± 20	54.63 ± 0.01	202 ± 10	2456604.64
s301_good_1175	classical belt	-	40.25 ± 0.01	0.104 ± 0.002	24.198 ± 0.001	211.6 ± 0.6	32.681 ± 0.002	112.3 ± 0.7	2456545.83
s240_good_3	classical belt	-	$40.3^{+0.1}_{-0.004}$	0.08 ± 0.01	22.55 ± 0.002	238 ± 20	43.49 ± 0.04	22 ± 20	2456877.66
s200_good_407	classical belt	-	$40.33^{+0.02}_{-0.05}$	0.06 ± 0.01	14.6 ± 0.03	101 ± 20	268.65 ± -0.04	323 ± 20	2456538.7
s200_good_743	classical belt	-	40.35 ± 0.003	0.07129 ± 5 × 10^{-5}	18.2052 ± 0.0003	154.5 ± 0.4	188.986 ± 0.0004	2.6 ± 0.3	2456546.74
2014 TF86	classical belt	-	40.421 ± 0.006	0.0782 ± 0.0002	32.0479 ± 0.0003	106.2 ± 0.2	65.0835 ± 0.0006	142.1 ± 0.2	2456931.58
s241_good_4	classical belt	-	40.5 ± 0.05	0.109 ± 0.006	38.464 ± 0.004	307.3 ± 0.9	87.574 ± 0.007	295.9 ± 0.2	2456903.64
2013 QP95	classical belt	-	40.6434 ± 0.0009	0.16937 ± 5 × 10^{-5}	25.4409 ± 0.0001	18.79 ± 0.01	71.3968 ± 0.0002	312.537 ± 0.005	2456534.7
s200_good_658	outer centaur	-	40.83 ± 0.02	0.2745 ± 0.0005	27.9843 ± 0.0002	193.4 ± 0.1	175.65086 ± 8 × 10^{-5}	339.32 ± 0.07	2456545.56
2015 TK363	classical belt	-	40.888 ± 0.003	0.0664 ± 0.0002	14.7881 ± 0.0002	174.36 ± 0.06	142.995 ± 0.001	60.21 ± 0.05	2456654.61
s242_good_7	classical belt	-	$40.971^{+0.009}_{-0.008}$	0.043 ± 0.0005	32.369 ± 0.002	255 ± 1	50.97 ± 0.001	17 ± 1	2456559.57

Table 1. continued from previous page

TNO ID	Class	Res.	a_b (AU)	e_b	i_b (deg)	ω_b (deg)	Ω_b (deg)	M_b (deg)	Epoch (JD)
(145452) 2005 RN43	classical belt	-	$41.512^{+0.008}_{-0.007}$	0.0225 ± 0.0003	19.2711 ± 0.0003	172 ± 2	186.9928 ± 0.0002	338 ± 2	2456543.64
2014 UF241	classical belt	-	41.516 ± 0.006	0.1591 ± 0.0003	26.75 ± 0.0009	18 ± 0.3	191.5667 ± -0.0004	169.5 ± 0.3	2456951.76
2014 PS70	classical belt	-	$41.7^{+0.3}_{-0.2}$	0.09 ± 0.02	15.1864 ± 0.003	308 ± 7	347.08 ± -0.03	51 ± 5	2457661.59
2014 VW37	classical belt	-	42.083 ± 0.002	$0.13267 \pm 7 \times 10^{-5}$	48.7849 ± 0.0002	255.5 ± 0.06	122.7768 ± 0.0003	16.64 ± 0.05	2456973.85
(503883) 2001 QF331	resonant	3:5	42.251 ± 0.009	0.2524 ± 0.0003	2.673 ± 0.0005	249.4 ± 0.1	156.785 ± 0.008	339.68 ± 0.05	2456544.7
2012 TC324	resonant	3:5	42.27 ± 0.002	$0.19703 \pm 3 \times 10^{-5}$	$9.631 \pm 4 \times 10^{-5}$	259.27 ± 0.02	131.8323 ± 0.0009	357.04 ± 0.01	2456569.7
2013 UT22	resonant	3:5	42.275 ± 0.002	$0.21235 \pm 8 \times 10^{-5}$	29.3413 ± 0.0001	138.47 ± 0.01	194.2379 ± 0.0002	44.05 ± 0.005	2456268.65
2013 TH172	resonant	3:5	42.313 ± 0.003	$0.25773 \pm 7 \times 10^{-5}$	11.5541 ± 0.0002	287.88 ± 0.02	42.6569 ± 0.0004	24.02 ± 0.01	2456568.61
2014 UD241	classical belt	-	42.331 ± 0.003	0.0498 ± 0.0002	12.4909 ± 0.0003	68.64 ± 0.09	40.6426 ± 0.0009	264.13 ± 0.08	2456619.64
2014 UE241	classical belt	-	42.476 ± 0.005	0.1234 ± 0.0002	7.5128 ± 0.0003	78.37 ± 0.09	60.419 ± 0.002	242.9 ± 0.1	2456569.66
2013 TD172	scattering	-	42.5 ± 0.1	0.163 ± 0.007	11.003 ± 0.001	85.4 ± 0.3	6.0387 ± 0.0004	294.5 ± 0.3	2456578.59
2013 RN109	classical belt	-	42.536 ± 0.003	0.1556 ± 9.00E-05	32.3057 ± 0.0002	17.89 ± 0.04	20.9369 ± 0.0001	336.06 ± 0.03	2456545.84
2003 SQ317	classical belt	-	42.659 ± 0.002	$0.08003 \pm 3 \times 10^{-5}$	28.5671 ± 0.0002	193.1 ± 0.09	$176.30698 \pm 5 \times 10^{-5}$	0.65 ± 0.08	2456537.85
2013 UQ15	classical belt	-	42.77 ± 0.002	0.113 ± 0.0001	27.3432 ± 0.0005	15.8 ± 0.2	189.1313 ± -0.0003	169.8 ± 0.2	2456932.79
2014 SN350	classical belt	-	42.82 ± 0.003	0.18878 ± 9.00E-05	32.0584 ± 0.0002	258.54 ± 0.04	171.6813 ± 0.0002	333.54 ± 0.02	2456925.78
s11_good_20	classical belt	-	42.82 ± 0.004	0.1711 ± 0.0001	22.7112 ± 0.0001	245.05 ± 0.08	107.6522 ± 0.0008	17.65 ± 0.05	2456888.86
2013 RF109	classical belt	-	42.864 ± 0.002	$0.06475 \pm 6 \times 10^{-5}$	9.7153 ± 0.0002	243.6 ± 0.1	144.8564 ± 0.0005	334.32 ± 0.09	2456537.84
s13_good_9	classical belt	-	42.899 ± 0.002	$0.16324 \pm 7 \times 10^{-5}$	32.8648 ± 0.0002	251.8 ± 0.08	140.8101 ± 0.0005	7.87 ± 0.06	2456920.84
2001 QO297	classical belt	-	42.933 ± 0.002	0.0365 ± 0.0002	1.1363 ± 0.0002	316.5 ± 0.06	143.319 ± 0.008	267.33 ± 0.06	2456543.69
2013 RP98	classical belt	-	42.934 ± 0.004	0.1318 ± 0.0002	13.288 ± 0.0001	177.85 ± 0.06	216.3248 ± 0.0009	306.75 ± 0.03	2456538.7
(160256) 2002 PD149	classical belt	-	42.954 ± 0.004	0.0615 ± 0.0003	4.9073 ± 0.0001	39 ± 0.2	103.551 ± 0.003	221.4 ± 0.2	2456543.69
(160256) 2002 PD149	classical belt	-	43 ± 1	0.06 ± 0.06	4.909 ± 0.007	38 ± 100	103.647 ± 0.008	222 ± 100	2456543.69
2003 QZ111	classical belt	-	43.008 ± 0.002	$0.06081 \pm 4 \times 10^{-5}$	2.6596 ± 0.0002	16.6 ± 0.2	326.046 ± 0.002	12.1 ± 0.1	2456565.63
2013 TB172	resonant candidate	7:12	43.033 ± 0.003	$0.19565 \pm 5 \times 10^{-5}$	11.6245 ± 0.0003	327.52 ± 0.08	35.2157 ± 0.0006	4.76 ± 0.05	2456578.71
2013 SG102	classical belt	-	43.072 ± -0.001	0.0074 ± 0.0001	7.9861 ± 0.0003	201 ± 2	200.565 ± 0.002	306.67 ± -0.06	2456565.62
2003 QM91	classical belt	-	43.1259 ± 0.0008	$0.04383 \pm 3 \times 10^{-5}$	3.0432 ± 0.0002	8.7 ± 0.2	8.064 ± -0.0002	350 ± 0.2	2456543.69
(385201) 1999 RN215	classical belt	-	43.1648 ± 0.0007	0.0733 ± 0.0003	12.4099 ± 0.0005	102.4 ± 0.3	140.65 ± 0.002	137.8 ± 0.4	2456931.84

Table 1. continued from previous page

TNO ID	Class	Res.	a_b (AU)	e_b	i_b (deg)	ω_b (deg)	Ω_b (deg)	M_b (deg)	Epoch (JD)
2013 RJ109	classical belt	-	43.32 ± 0.005	0.1318 ± 0.0004	20.2991 ± 0.0002	253.57 ± 0.06	182.4743 ± 0.0002	286.25 ± 0.02	2456543.66
(471954) 2013 RM98	classical belt	-	43.329 ± 0.005	0.1313 ± 0.0003	28.0859 ± 0.0003	252.68 ± 0.06	352.43819 ± -9.00E-05	94.47 ± 0.08	2456543.67
s301_good_1073	classical belt	-	43.3342 ± 0.0002	0.0592 ± 0.0003	4.2203 ± 0.0003	90 ± 1	98.73 ± 0.01	184 ± 1	2456578.68
s200_good_25	classical belt	-	43.4 ± 0.2	0.15 ± 0.01	6.236 ± 0.001	117 ± 4	283.68 ± 0.02	317 ± 2	2457614.77
s301_good_2580	classical belt	-	43.428 ± 0.001	0.0379 ± 0.0002	4.1259 ± 0.0003	174.3 ± 0.3	44.304 ± 0.003	141.7 ± 0.4	2456546.8
2013 SK102	classical belt	-	43.482 ± 0.003	0.1837 ± 0.0002	7.4184 ± 0.0002	151.4 ± 0.1	66.342 ± 0.003	134 ± 0.1	2456563.62
2014 QU495	resonant	4:7	43.527 ± 0.005	0.2635 ± 0.0002	21.2897 ± 0.0002	170.21 ± 0.03	177.5986 ± 0.0003	22.17 ± 0.02	2456887.86
2013 VZ31	classical belt	-	43.53 ± 0.005	0.1171 ± 0.0003	2.6737 ± 0.0001	138.8 ± 0.2	74.856 ± 0.008	139.2 ± 0.2	2456604.66
s302_good_82	classical belt	-	43.54 ± 0.001	0.09362 $\pm 7 \times 10^{-5}$	10.0144 ± 0.0001	281.9 ± 0.2	117.109 ± 0.002	347.9 ± 0.2	2456568.79
s118_good_10	classical belt	-	43.552 ± 0.003	0.0719 ± 0.0007	35.806 ± 0.0005	47.1 ± 0.2	72.238 ± 0.001	261.1 ± 0.1	2457017.64
2014 TL95	resonant	4:7	43.556 ± 0.004	0.1881 ± 0.0001	10.5949 ± 0.0001	307.06 ± 0.07	100.919 ± 0.002	344.64 ± 0.04	2456931.84
(119956) 2002 PA149	resonant	4:7	43.587 ± 0.004	0.174 ± 0.0003	4.04955 $\pm 8 \times 10^{-5}$	153.1 ± 0.02	105.579 ± 0.004	81.91 ± 0.04	2456537.78
s200_good_481	resonant candidate	4:7	$43.6^{+0.03}_{-0.05}$	0.124 ± 0.004	11.63 ± 0.02	234 ± 10	297.65 ± -0.02	172 ± 10	2456548.67
2013 SJ102	resonant	4:7	43.617 ± 0.004	0.27648 $\pm 8 \times 10^{-5}$	7.34556 $\pm 2 \times 10^{-5}$	315.52 ± 0.01	93.723 ± 0.001	334.381 ± 0.005	2456563.62
2013 RE109	resonant	4:7	43.649 ± 0.002	0.1519 ± 0.0002	5.41702 $\pm 5 \times 10^{-5}$	165.33 ± 0.02	112.863 ± 0.002	72.9 ± 0.01	2456537.79
s301_good_1198	resonant candidate	4:7	43.7 ± 0.1	0.177 ± 0.005	2.3817 ± 0.0002	250 ± 2	80.72 ± 0.01	26 ± 1	2456546.8
2001 QE298	resonant	4:7	43.71 ± 0.01	0.1552 ± 0.0001	3.6584 ± 0.0004	10.7 ± 0.1	7.75572 ± -3×10^{-5}	352 ± 0.1	2456593.57
2013 TF172	classical belt	-	43.752 ± 0.004	0.0249 ± 0.0002	2.8936 ± 0.0002	314.2 ± 0.3	126.995 ± 0.005	284.4 ± 0.2	2456578.63
(307616) 2003 QW90	classical belt	-	43.765 ± 0.005	0.0764 ± 0.0008	10.359 ± 0.0007	87.23 ± 0.05	17.7681 ± 0.0003	275.01 ± 0.09	2456618.58
2013 TL172	classical belt	-	43.78 ± 0.003	0.0611 ± 0.0001	1.7911 $\pm 2 \times 10^{-5}$	76.3 ± 0.3	95.08 ± 0.01	193 ± 0.3	2456578.61
s301_good_1491	classical belt	-	43.896 ± 0.007	0.088 ± 0.0004	4.5865 ± 0.0005	176.4 ± 0.5	35.07 ± 0.003	150.2 ± 0.5	2456578.61
2014 VV39	classical belt	-	43.938696 $\pm 10^{-5}$	0.0137 ± 0.0001	1.6287 ± 0.0001	282.2 ± 0.5	136.321 ± 0.006	310.3 ± 0.2	2456546.8
2001 QQ322	classical belt	-	43.991 ± 0.002	0.0518 ± 0.0002	3.95831 $\pm 8 \times 10^{-5}$	350.6 ± 0.09	76.478 ± 0.003	297.74 ± 0.05	2456544.71
s301_good_1446	classical belt	-	44.008 ± -0.007	0.0826 ± 0.0004	2.9743 ± 0.0003	322 ± 2	30.279 ± 0.001	13 ± 2	2456604.67
2001 QS322	classical belt	-	44.02441 $\pm 5 \times 10^{-5}$	0.03869 $\pm 4 \times 10^{-5}$	0.247 ± 0.0004	359.4 ± 0.5	348.46 ± 0.01	15.4 ± 0.5	2456565.66
2013 RO109	classical belt	-	44.037 ± 0.001	0.03526 $\pm 6 \times 10^{-5}$	1.5237 ± 0.0002	328.3 ± 0.3	52.095 ± 0.007	341.7 ± 0.3	2456546.8
s200_good_80	outer centaur	-	44.1 ± 0.2	0.478 ± 0.003	5.0961 ± 0.0008	275.9 ± 0.3	302.259 ± 0.003	75.4 ± 0.7	2456540.63
s200_good_750	classical belt	-	44.1 ± 0.6	0.16 ± 0.05	18.29 ± 0.03	95 ± 10	181.22 ± 0.05	41 ± 9	2456540.58
s301a_good_324	classical belt	-	44.14 ± -0.01	0.0113 ± -0.0002	1.5949 ± 0.0002	313 ± 2	63.17 ± 0.01	346 ± 2	2456578.61

Table 1. continued from previous page

TNO ID	**Class**	**Res.**	a_b **(AU)**	e_b	i_b **(deg)**	ω_b **(deg)**	Ω_b **(deg)**	M_b **(deg)**	**Epoch (JD)**
2013 WG114	classical belt	-	44.151 ± 0.005	0.06413 ± 9.00E-05	1.4709 ± 0.0001	273.6 ± 0.2	70.02 ± 0.01	16 ± 0.2	2456618.57
s302_good_3	classical belt	-	44.251 ± 0.006	0.1199 ± 0.0001	11.2737 ± 0.0001	280.1 ± 0.1	114.575 ± 0.002	350.29 ± 0.09	2456568.79
2014 OD394	classical belt	-	44.365 ± 0.002	0.0954 ± 0.0002	11.2482 ± 0.0003	82.6 ± 0.1	130.2 ± 0.001	149.3 ± 0.1	2456576.73
2015 RT245	classical belt	-	44.384 ± 0.002	0.0841 ± 0.0001	0.9578 ± 0.0002	343.4 ± 0.1	330.387 ± 0.007	42.18 ± 0.08	2456577.62
2014 VV39	classical belt	-	44.45 ± -0.01	0.0219 ± -0.0002	1.6383 ± 0.0004	239 ± 2	136.74 ± 0.02	352 ± 2	2456546.8
s301_good_300	classical belt	-	44.63 ± -0.01	0.0233 ± -0.0002	1.1637 ± 0.0002	320 ± 2	49.154 ± 0.007	359 ± -400	2456563.61
2013 RP109	classical belt	-	44.703 ± 0.002	0.10351 ± 4 × 10^{-5}	2.35056 ± 3 × 10^{-5}	269.37 ± 0.06	105.547 ± 0.005	351.16 ± 0.05	2456546.8
s240_good_7	classical belt	-	44.77 ± 0.03	0.1391 ± 0.0005	34.3239 ± 0.0002	326.2 ± 0.1	3.2324 ± 0.0008	334.7 ± 0.09	2456538.55
2013 RS109	classical belt	-	44.8 ± 0.2	0.13 ± 0.01	4.8469 ± 0.0003	305 ± 2	353.502 ± -0.004	47.9 ± 0.9	2456537.76
2016 SV58	scattering	-	44.915 ± 0.005	0.2672 ± 0.0001	13.59559 ± 6 × 10^{-5}	305.7 ± 0.03	132.576 ± 0.001	333.16 ± 0.02	2456953.8
2001 QO297	classical belt	-	45 ± 2	0.15 ± 0.08	1.138 ± 0.008	305 ± 2	143.4 ± 0.3	292 ± 7	2456543.69
2001 QP297	classical belt	-	45.205 ± 0.004	0.1206 ± 0.0003	1.43081 ± 8 × 10^{-5}	164.1 ± 0.04	111.81 ± 0.01	77.22 ± 0.03	2456578.61
2015 PF312	classical belt	-	45.2649 ± 0.0006	0.09081 ± 2 × 10^{-5}	17.9941 ± 5 × 10^{-5}	260.23 ± 0.02	160.6353 ± 0.0003	337.97 ± 0.02	2456247.58
2013 RX108	classical belt	-	45.295 ± 0.003	0.0593 ± 0.0002	4.8705 ± 0.0001	31.76 ± 0.03	71.754 ± 0.002	277.69 ± 0.04	2456537.86
s301_good_946	classical belt	-	45.31 ± 0.004	0.1718 ± 0.0008	16.9 ± 0.001	336 ± 1	21.2301 ± 0.0008	11.1 ± 0.8	2456564.73
s200_good_198	classical belt	-	45.338 ± 0.005	0.1573 ± 0.0002	15.1767 ± 0.0003	78 ± 0.03	184.3703 ± 0.0002	73.21 ± 0.03	2456546.77
s301_good_1346	classical belt	-	45.348 ± 0.002	0.08049 ± 4 × 10^{-5}	1.18649 ± 4 × 10^{-5}	249.8 ± 0.2	109.14 ± 0.01	7.6 ± 0.2	2456563.61
2013 TZ171	classical belt	-	45.367 ± 0.004	0.19211 ± 7 × 10^{-5}	15.8862 ± 0.0002	241.31 ± 0.06	163.6584 ± 0.0006	349.44 ± 0.04	2456569.79
2013 RY108	outer centaur	-	45.53 ± 0.02	0.4609 ± 0.0003	10.75959 ± 3 × 10^{-5}	5.171 ± 0.009	93.27 ± 0.001	321.074 ± 0.008	2456545.83
2014 TB86	classical belt	-	45.56 ± 0.002	0.17687 ± 4 × 10^{-5}	19.113 ± 0.0002	330.56 ± 0.03	50.2367 ± 0.0004	353.48 ± 0.02	2456545.84
2014 TB86	classical belt	-	45.562 ± 0.002	0.17691 ± 3 × 10^{-5}	19.1129 ± 0.0001	330.57 ± 0.02	50.2367 ± 0.0003	353.47 ± 0.02	2456545.84
s301_good_127	classical belt	-	45.598 ± 0.003	0.14412 ± 6 × 10^{-5}	6.4625 ± 0.0001	269.76 ± 0.06	67.99 ± 0.002	14.41 ± 0.04	2456546.73
2014 QF442	classical belt	-	45.9 ± 0.008	0.2071 ± 0.0003	30.5067 ± 8 × 10^{-5}	246.4 ± 0.2	52.9177 ± 0.0009	13 ± 0.1	2456885.73
s14_good_1	classical belt	-	46.066 ± 0.008	0.1587 ± 0.0005	29.9093 ± 0.0001	339.54 ± 0.07	131.1873 ± 0.0009	309.76 ± 0.03	2456916.86
2015 TJ363	classical belt	-	46.132 ± 0.003	0.1807 ± 0.0001	14.33619 ± 9.00E-05	354.15 ± 0.02	97.386 ± 0.001	309.46 ± 0.01	2456569.7
s200_good_615	scattering	-	46.312 ± 0.008	0.3436 ± 0.0001	14.3886 ± 0.0001	86.49 ± 0.02	202.6127 ± 0.0005	16.486 ± 0.009	2456543.63

Table 1. continued from previous page

TNO ID	**Class**	**Res.**	a_b **(AU)**	e_b	i_b **(deg)**	ω_b **(deg)**	Ω_b **(deg)**	M_b **(deg)**	**Epoch (JD)**
2013 TK172	classical belt	-	46.459 ± 0.006	0.2041 ± 0.0003	12.5919 ± 0.0002	246.95 ± 0.06	71.977 ± 0.001	39.01 ± 0.03	2456569.67
2013 TM159	classical belt	-	46.468 ± 0.003	$0.16791 \pm 6 \times 10^{-5}$	$9.54264 \pm 7 \times 10^{-5}$	294.31 ± 0.05	107.96 ± 0.001	347.88 ± 0.03	2456568.75
s301d_good_25	classical belt	-	46.62 ± 0.01	0.1464 ± 0.0007	23.726 ± 0.001	95.7 ± 0.2	37.028 ± 0.001	252.5 ± 0.2	2456933.8
2011 SW281	classical belt	-	46.655 ± 0.004	0.0949 ± 0.0001	$4.63342 \pm 5 \times 10^{-5}$	302.61 ± 0.07	111.086 ± 0.003	323.11 ± 0.05	2456569.66
s200_good_540	classical belt	-	46.68 ± 0.08	0.166 ± 0.005	21.6188 ± 0.0004	61.5 ± 0.3	$179.90758 \pm 6 \times 10^{-5}$	77.2 ± 0.7	2456548.68
2014 RJ70	classical belt	-	46.88 ± 0.01	0.189 ± 0.0002	$26.47783 \pm 2 \times 10^{-5}$	274.9 ± 0.1	30.8855 ± 0.0007	358.65 ± 0.07	2456912.56
s301_good_160	classical belt	-	47 ± 0.3	0.2 ± 0.02	13.356 ± 0.005	357 ± 300	43.338 ± 0.001	336 ± 7	2457639.86
(483002) 2014 QS441	classical belt	-	47.0073 ± 0.0008	$0.08342 \pm 8 \times 10^{-5}$	37.8853 ± 0.0001	267.61 ± 0.04	185.9271 ± 0.0001	306.63 ± 0.02	2456594.65
2013 SS102	classical belt	-	47.258 ± 0.004	0.1968 ± 0.0001	26.3777 ± 0.0002	19.65 ± 0.04	21.5278 ± 0.0001	333.62 ± 0.02	2456565.67
s301_good_798	classical belt	-	47.49 ± 0.01	0.2018 ± 0.0005	$6.68053 \pm 7 \times 10^{-5}$	20.38 ± 0.07	96.327 ± 0.006	274.8 ± 0.1	2456974.63
(137295) 1999 RB216	resonant	1:2	47.547 ± 0.003	$0.29237 \pm 3 \times 10^{-5}$	12.6879 ± 0.0002	208.67 ± 0.02	175.7239 ± 0.0004	359.31 ± 0.01	2456545.87
2012 WE37	resonant	1:2	47.648 ± 0.005	$0.24566 \pm 6 \times 10^{-5}$	25.6882 ± 0.0003	331.06 ± 0.05	59.8663 ± 0.0004	0.06 ± 0.03	2456247.63
(145452) 2005 RN43	outer centaur	-	47.67 ± 0.04	0.671 ± 0.0003	33.258 ± 0.0005	289.7 ± 0.03	172.678 ± 0.0003	314.01 ± 0.02	2456575.59
(495189) 2012 VR113	resonant	1:2	47.692 ± 0.002	$0.17188 \pm 7 \times 10^{-5}$	$19.28378 \pm 3 \times 10^{-5}$	220.45 ± 0.02	121.0325 ± 0.0005	35.16 ± 0.01	2456242.66
2013 TG172	resonant candidate	1:2	47.88 ± 0.01	0.3196 ± 0.0002	4.8011 ± 0.0004	339.44 ± 0.05	14.472 ± 0.0005	6.18 ± 0.02	2456568.59
2013 RR109	classical belt	-	48.01 ± 0.03	0.066 ± 0.005	4.237 ± 0.002	90 ± 5	225.8 ± 0.02	28 ± 5	2456546.76
2013 TE172	detached	-	48.255 ± 0.003	$0.26045 \pm 4 \times 10^{-5}$	29.841 ± 0.0002	325.68 ± 0.03	50.8138 ± 0.0002	2.8 ± 0.01	2456569.77
2016 TY94	detached	-	48.855 ± 0.004	$0.24573 \pm 5 \times 10^{-5}$	25.6687 ± 0.0001	279.1 ± 0.07	108.7249 ± 0.0005	355.81 ± 0.04	2456930.75
2012 WG37	scattering	-	49.015 ± 0.009	0.3435 ± 0.0002	14.3201 ± 0.0002	41.17 ± 0.02	106.999 ± 0.002	288.17 ± 0.04	2456250.62
(534073) 2014 QL441	detached	-	49.1 ± 0.5	0.27 ± 0.02	26.27 ± 0.02	285 ± 6	75.85 ± 0.04	14 ± 3	2456887.77
2010 JJ210	detached	-	49.28 ± 0.08	0.249 ± 0.002	7.1674 ± 0.0005	101.6 ± 0.7	215.93 ± 0.004	17.1 ± 0.4	2456543.66
s200_good_569	detached	-	49.4 ± 0.6	0.29 ± 0.02	5.617 ± 0.001	135 ± 1	291.05 ± 0.03	316.3 ± 0.1	2456545.79
2016 SP56	detached	-	49.64 ± 0.01	0.257 ± 0.0002	20.0422 ± 0.0003	30.74 ± 0.04	75.2708 ± 0.0008	313.33 ± 0.02	2456888.89
s119_good_0	classical belt	-	$50^{+1}_{-0.2}$	0.18 ± 0.01	37.56 ± 0.03	258 ± 200	105.6 ± 0.3	3 ± 80	2457327.73
2013 RJ109	detached	-	50.1 ± 0.6	0.35 ± 0.01	18.894 ± 0.002	246.3 ± 0.2	183.648 ± 0.001	314.7 ± 0.4	2456576.6
2013 RR98	detached	-	50.214 ± 0.005	0.2854 ± 0.0001	$37.76095 \pm 5 \times 10^{-5}$	233.46 ± 0.02	62.266 ± 0.0003	19.851 ± 0.009	2456548.76
2013 TX171	resonant	6:13	50.363 ± 0.007	$0.27665 \pm 8 \times 10^{-5}$	19.5889 ± 0.0003	203.66 ± 0.06	167.372 ± 0.0003	358.63 ± 0.03	2456569.66
2013 RM109	resonant	5:11	50.83 ± 0.01	0.2229 ± 0.0008	14.2853 ± 0.0003	128.6 ± 0.2	261.019 ± 0.001	318.08 ± 0.07	2456545.69

Table 1. continued from previous page

TNO ID	Class	Res.	a_b (AU)	e_b	i_b (deg)	ω_b (deg)	Ω_b (deg)	M_b (deg)	Epoch (JD)
2013 RL109	outer centaur	-	51.3 ± 0.5	0.42 ± 0.01	12.6721 ± 0.0006	75 ± 1	199.184 ± 0.002	25.8 ± 0.1	2456575.59
2015 AS293	resonant	4:9	51.58 ± 0.02	0.3614 ± 0.0004	34.4326 ± 0.0001	192.68 ± 0.01	88.3938 ± 0.0009	44.62 ± 0.01	2457034.55
s301_good_1002	detached	-	51.6 ± 0.2	0.344 ± 0.004	20.8762 ± 0.0009	67.3 ± 0.2	191.801 ± -0.001	64.2 ± 0.4	2456958.66
2013 TJ172	detached	-	51.93 ± 0.005	0.28859 ± 9.00E-05	27.3788 ± 0.0002	248.23 ± 0.02	176.5228 ± 0.0002	337.21 ± 0.01	2456568.79
s200_good_190	classical belt	-	52.01 ± 0.02	0.2219 ± 0.0004	12.1677 ± 0.0004	114.02 ± 0.07	186.1537 ± 0.0004	34.75 ± 0.04	2456546.77
2013 SM102	detached	-	52.284 ± 0.006	0.25582 ± 8 × 10^{-5}	11.4072 ± 0.0002	226.98 ± 0.03	154.0146 ± 0.0006	353.27 ± 0.02	2456563.62
(529823) 2010 PP81	detached	-	52.45 ± 0.03	0.2804 ± 0.0002	30.7725 ± 0.0001	174.9 ± 0.7	172.2209 ± -0.0007	355.4 ± 0.4	2456543.66
s240_good_0	detached	-	52.61 ± 0.03	0.2738 ± 0.0007	28.19157 ± 6 × 10^{-5}	321.03 ± 0.08	38.244 ± 0.001	324.41 ± 0.03	2457277.51
2013 SR102	resonant	3:7	52.85 ± 0.03	0.3835 ± 0.0005	29.92055 ± 9.00E-05	9.76 ± 0.05	41.445 ± 0.001	298.51 ± 0.04	2456565.5
2013 RO98	detached	-	53 ± 5	0.3 ± 0.1	18.9 ± 0.1	90 ± 20	292.9 ± 0.2	333 ± 8	2456540.57
s302_good_31	resonant	3:7	53.045 ± 0.005	0.37415 ± 5 × 10^{-5}	9.9852 ± 6 × 10^{-5}	276.32 ± 0.03	109.98 ± 0.001	0.63 ± 0.01	2456544.87
(495297) 2013 TJ159	resonant	3:7	53.089 ± 0.005	0.3173 ± 9.00E-05	4.8066 ± 0.0002	174.21 ± 0.04	165.1691 ± 0.0009	11.27 ± 0.02	2456546.81
2014 QG442	detached	-	53.7 ± 0.2	0.365 ± 0.004	30.455 ± 0.001	242 ± 0.4	95.897 ± 0.002	27.63 ± 0.09	2456888.92
s200_good_168	scattering	-	54.18 ± 0.03	0.3984 ± 0.0005	18.0483 ± 0.0003	81.25 ± 0.02	188.996 ± 0.0006	29.35 ± 0.006	2456548.66
2014 NB66	classical belt	-	55 ± 6	0.2 ± 0.1	4.69 ± 0.08	114 ± 10	297 ± 1	319 ± 9	2457614.78
s200_good_806	outer centaur	-	55.06 ± 0.08	0.6582 ± 0.0007	7.3774 ± 0.0004	297.07 ± 0.03	290.812 ± 0.004	39.04 ± 0.04	2456576.59
(495190) 2012 VS113	detached	-	55.068 ± 0.002	0.30928 ± 2 × 10^{-5}	26.78573 ± 7 × 10^{-5}	220.138 ± 0.008	171.6043 ± 0.0002	1.716 ± 0.004	2456243.66
s302_good_124	resonant candidate	2:5	55.3 ± 0.2	0.446 ± 0.003	15.068 ± 0.001	187.9 ± 0.5	170.096 ± 0.004	15.6 ± 0.1	2456619.71
2013 RZ108	resonant	2:5	55.38 ± 0.02	0.4525 ± 0.0003	13.0319 ± 0.0005	333.6 ± 0.2	65.597 ± 0.002	355.34 ± 0.06	2456545.85
2014 YL50	resonant	2:5	55.451 ± 0.008	0.3251 ± 0.0001	29.1463 ± 0.0001	234.34 ± 0.04	127.3833 ± 0.0005	12.7 ± 0.02	2457007.68
s12_good_4	resonant	2:5	55.49 ± 0.04	0.359 ± 0.001	32.116 ± 0.001	338.7 ± 0.4	89.063 ± 0.003	341.9 ± 0.1	2456961.78
2015 RW245	outer centaur	-	56.5 ± 0.1	0.531 ± 0.001	13.305 ± 0.001	19.5 ± 0.6	0.39362 ± 7 × 10^{-5}	356.2 ± 0.1	2456578.59
2014 QT495	scattering	-	57.134 ± 0.005	0.4739 ± 4 × 10^{-5}	44.6744 ± 5 × 10^{-5}	258.73 ± 0.01	103.7911 ± 0.0003	1.537 ± 0.005	2456891.85
s118_good_6	detached	-	57.7 ± 0.1	0.349 ± 0.004	29.964 ± 0.001	344 ± 0.7	76.068 ± 0.006	335.7 ± 0.2	2457251.91
2014 PM82	detached	-	58 ± 2	0.41 ± 0.04	23.8 ± 0.09	305 ± 5	358.412 ± -0.003	23 ± 1	2456546.77
2014 UN225	detached	-	59.2 ± 0.04	0.3465 ± 0.0007	53.1497 ± 0.0001	323.42 ± 0.02	68.6908 ± 0.0006	322.66 ± 0.01	2456952.51
s200_good_466	detached	-	59.7 ± 0.8	0.4 ± 0.01	8.393 ± 0.001	37 ± 2	255.57 ± 0.02	21.3 ± 0.4	2456548.68
2014 RS63	detached	-	60 ± 2	0.39 ± 0.03	28.978 ± 0.009	314 ± 7	38.91 ± 0.08	347 ± 3	2456904.69
s200_good_175	detached	-	60.3 ± 0.6	0.32 ± 0.02	11.9467 ± 0.0009	213 ± 4	186.3212 ± 0.0008	336 ± 1	2456565.62

Table 1. continued from previous page

TNO ID	**Class**	**Res.**	a_b **(AU)**	e_b	i_b **(deg)**	ω_b **(deg)**	Ω_b **(deg)**	M_b **(deg)**	**Epoch (JD)**
s302_good_160	detached	-	60.99 ± 0.03	0.3969 ± 0.0003	14.1896 ± 0.0002	334.77 ± 0.03	76.795 ± 0.001	345.962 ± 0.009	2456568.79
s200_good_272	detached	-	61.19 ± 0.06	0.416 ± 0.001	25.2551 ± 0.0002	112.3 ± 0.2	176.1569 ± 0.0001	14.94 ± 0.06	2456546.7
s301_good_720	detached	-	61.53 ± 0.007	$0.37693 \pm 8 \times 10^{-5}$	5.4668 ± 0.0002	181.18 ± 0.03	156.353 ± 0.001	11.9 ± 0.01	2456568.59
2013 VQ25	detached	-	61.547 ± 0.006	$0.42287 \pm 6 \times 10^{-5}$	28.5944 ± 0.0002	215.05 ± 0.03	153.6874 ± 0.0003	3.91 ± 0.01	2456888.85
2014 OQ394	detached	-	61.962 ± 0.005	$0.43965 \pm 4 \times 10^{-5}$	29.4887 ± 0.0002	157.85 ± 0.01	$186.62073 \pm 3 \times 10^{-5}$	7.444 ± 0.004	2456544.7
(134210) 2005 PQ21	detached	-	61.99 ± 0.01	0.3931 ± 0.0001	6.482 ± 0.0002	22.18 ± 0.03	316.3337 ± 0.0009	4.44 ± 0.01	2456540.62
2014 SP363	detached	-	62.409 ± 0.007	0.3152 ± 0.0002	31.2281 ± 0.0003	267.8 ± 0.06	145.4485 ± 0.0005	341.37 ± 0.02	2456982.7
2010 TJ	detached	-	62.856 ± 0.006	0.365 ± 0.0001	38.9009 ± 0.0002	273.92 ± 0.03	91.2989 ± 0.0004	9.9 ± 0.01	2456887.91
s13_good_7	detached	-	65.14 ± 0.02	0.4398 ± 0.0003	28.5578 ± 0.0001	230 ± 0.04	129.5521 ± 0.0007	15.69 ± 0.01	2456927.82
2013 SG102	outer centaur	-	65.7 ± 0.4	0.62 ± 0.003	8.1699 ± 0.0006	51.74 ± 0.03	199.722 ± 0.002	26.77 ± 0.09	2456565.62
(480017) 2014 QB442	detached	-	66.34 ± 0.01	0.4478 ± 0.0001	7.2913 ± 0.0002	269.32 ± 0.02	75.295 ± 0.002	12.82 ± 0.006	2456568.64
s14_good_4	detached	-	67.22 ± 0.01	0.3587 ± 0.0003	32.478 ± 0.0003	287.4 ± 0.1	149.5281 ± 0.0009	346.89 ± 0.04	2456904.9
2013 SN102	detached	-	67.72 ± 0.01	$0.43879 \pm 8 \times 10^{-5}$	$4.45459 \pm 5 \times 10^{-5}$	247.36 ± 0.02	114.147 ± 0.002	1.153 ± 0.007	2456564.73
(136199) Eris	detached	-	67.83 ± 0.03	0.4384 ± 0.0004	43.993 ± 0.001	151.2 ± 0.2	35.976 ± 0.001	202.7 ± 0.2	2456547.89
s301_good_988	scattering	-	69 ± 5	0.54 ± 0.04	11.3 ± 0.1	42 ± 2	8.69 ± 0.03	349.3 ± 0.3	2456887.82
2014 QC442	detached	-	69.09 ± 0.02	0.5008 ± 0.0001	18.99 ± 0.0002	45.035 ± 0.007	46.6736 ± 0.0003	335.608 ± 0.002	2456568.64
s12_good_5	resonant	2:7	69.18 ± 0.08	0.5099 ± 0.0009	28.2758 ± 0.0003	294.5 ± 0.2	130.862 ± 0.001	349.85 ± 0.05	2457003.7
2015 TW361	resonant	2:7	69.27 ± 0.009	$0.46808 \pm 6 \times 10^{-5}$	16.6857 ± 0.0002	331.652 ± 0.009	42.2079 ± 0.0002	359.956 ± 0.003	2456569.66
2016 SE56	resonant	2:7	69.5 ± 0.01	$0.55324 \pm 8 \times 10^{-5}$	26.7798 ± 0.0001	218.799 ± 0.009	175.1145 ± 0.0001	356.576 ± 0.002	2456568.63
2013 TM172	detached	-	69.697 ± 0.009	$0.4773 \pm 6 \times 10^{-5}$	12.6083 ± 0.0002	352.313 ± 0.009	14.8665 ± 0.0001	358.455 ± 0.003	2456578.63
s302_good_132	outer centaur	-	72.24 ± 0.07	0.6788 ± 0.0004	17.8937 ± 0.0003	345.64 ± 0.08	63.0945 ± 0.0007	356.97 ± 0.01	2456568.75
2016 SS55	detached	-	73.15 ± 0.02	0.4761 ± 0.0001	28.4964 ± 0.0002	158.01 ± 0.02	182.7956 ± 0.0002	16.69 ± 0.003	2456568.79
(145480) 2005 TB190	detached	-	75.66 ± 0.01	$0.38939 \pm 7 \times 10^{-5}$	26.4795 ± 0.0002	171.44 ± 0.03	$180.4517 \pm 6 \times 10^{-5}$	358.24 ± 0.01	2456540.62
2014 SO350	resonant	1:4	75.8 ± 0.008	$0.54352 \pm 5 \times 10^{-5}$	$24.04237 \pm 6 \times 10^{-5}$	244.161 ± 0.009	140.9972 ± 0.0004	0.866 ± 0.002	2456930.76
2008 UA332	resonant	1:4	75.83 ± 0.02	0.5134 ± 0.0002	30.7411 ± 0.0002	226.49 ± 0.01	109.0105 ± 0.0006	18.71 ± 0.002	2456915.83
2014 QV495	detached	-	79.56 ± 0.05	0.5448 ± 0.0004	23.3893 ± 0.0003	276.98 ± 0.08	69.197 ± 0.001	5.75 ± 0.02	2456888.83
s11_good_14	outer centaur	-	80.8 ± 0.2	0.707 ± 0.0008	37.132 ± 0.0008	215 ± 0.2	167.677 ± 0.0004	0.23 ± 0.03	2457318.74
2013 SS102	scattering	-	82.4 ± 0.2	0.581 ± 0.001	19.7477 ± 0.0004	10.66 ± 0.05	27.9211 ± 0.0005	351.778 ± 0.009	2456578.73
2013 RJ109	detached	-	83.06 ± 0.08	0.526 ± 0.0004	14.1241 ± 0.0003	145.1 ± 0.04	189.4148 ± 0.0004	3.52 ± 0.01	2456576.6
s12_good_0	detached	-	85.75 ± 0.02	$0.60443 \pm 8 \times 10^{-5}$	$22.90037 \pm 8 \times 10^{-5}$	277.14 ± 0.02	108.86 ± 0.0006	0.255 ± 0.004	2456931.88

Table 1. continued from previous page

TNO ID	Class	Res.	a_b (AU)	e_b	i_b (deg)	ω_b (deg)	Ω_b (deg)	M_b (deg)	Epoch (JD)
2013 RK109	scattering	-	89.48 ± 0.02	0.61695 ± 7×10^{-5}	12.8486 ± 0.0001	162.35 ± 0.01	176.759 ± 0.0002	6.04 ± 0.002	2456544.72
s200_good_122	scattering	-	90.01 ± 0.04	0.6316 ± 0.0002	17.1525 ± 0.0001	86.9 ± 0.01	192.4784 ± 0.0004	8.626 ± 0.001	2456538.68
2013 SO102	outer centaur	-	90.5 ± 0.1	0.6754 ± 0.0003	9.4718 ± 0.0002	237.3 ± 0.1	141.268 ± 0.002	0.86 ± 0.02	2456951.77
2013 SQ102	resonant candidate	3:16	91.65 ± 0.07	0.6162 ± 0.0004	29.5484 ± 0.0001	357.64 ± 0.02	14.306 ± 0.0006	343.301 ± 0.002	2456565.5
(145474) 2005 SA278	scattering	-	92.24 ± 0.02	0.64155 ± 7×10^{-5}	16.2753 ± 9.00E-05	277.083 ± 0.007	170.3535 ± 0.0004	350.2161 ± 0.0008	2456268.65
2014 XY40	outer centaur	-	92.9 ± 0.2	0.693 ± 0.001	28.987 ± 0.0004	336.87 ± 0.02	132.529 ± 0.002	338.8 ± 0.02	2456982.7
s200_good_248	outer centaur	-	95.6 ± 0.2	0.7396 ± 0.0006	13.5922 ± 0.0005	79.43 ± 0.02	185.2107 ± 0.0003	13.434 ± 0.005	2456544.67
(437360) 2013 TV158	outer centaur	-	97 ± 3	0.73 ± 0.01	41.11 ± 0.02	285.8 ± 0.1	191.44 ± 0.02	348.56 ± 0.07	2456930.78
s302_good_44	outer centaur	-	100 ± 6	0.71 ± 0.02	18.0226 ± 0.0007	291.9 ± 0.9	177.076 ± 0.005	349.31 ± 0.05	2456594.67
2014 SR350	detached	-	101 ± 1	0.636 ± 0.005	28.76629 ± 6×10^{-5}	220 ± 0.3	35.124 ± 0.003	11.9939 ± 0.0003	2456886.71
s17_good_0	detached	-	104.83 ± 0.03	0.5213 ± 0.0002	43.1491 ± 6×10^{-5}	297.15 ± 0.03	130.3806 ± 0.0005	351.796 ± 0.006	2456925.82
2014 UZ224	detached	-	108.8 ± 0.8	0.648 ± 0.003	26.7846 ± -0.0003	29.4 ± 0.2	131 ± 0.002	319.4 ± 0.2	2456888.92
(437360) 2013 TV158	detached	-	111.229 ± 0.006	0.67212 ± 2×10^{-5}	31.14327 ± 8×10^{-5}	232.106 ± 0.004	181.0751 ± 0.0001	357.306 ± 0.0005	2456575.64
s200_good_624	outer centaur	-	111.7 ± 0.4	0.7652 ± 0.0009	10.2728 ± 0.0002	142.63 ± 0.01	285.697 ± 0.002	348.754 ± 0.006	2456564.67
s302_good_209	scattering	-	116 ± 5	0.68 ± 0.02	18.59 ± 0.03	272 ± 20	120 ± 0.2	1 ± 3	2456619.75
s200_good_461	detached	-	120.84 ± 0.04	0.669 ± 0.0001	31.6747 ± 0.0002	160.02 ± 0.01	175.66083 ± 10^{-5}	2.144 ± 0.001	2456543.67
2014 QW495	scattering	-	133.5 ± 0.2	0.7474 ± 0.0004	28.5047 ± 0.0002	208.87 ± 0.02	75.9361 ± 0.0005	2.186 ± 0.002	2456898.55
s200_good_520	scattering	-	158.4 ± 0.1	0.7686 ± 0.0002	17.3988 ± 0.0001	27.39 ± 0.02	293.4378 ± 0.0003	1.223 ± 0.002	2456540.57
s200_good_30	detached	-	160 ± 20	0.71 ± 0.04	4.81 ± 0.05	130 ± 40	219.4 ± 0.7	0 ± 5	2457657.63
(508338) 2015 SO20	scattering	-	164.8 ± 0.2	0.7988 ± 0.0003	23.4104 ± 0.0005	354.8 ± 0.1	33.6343 ± 0.0004	359.322 ± 0.009	2456545.85
2016 QV89	detached	-	171.64 ± 0.05	0.76722 ± 8×10^{-5}	21.38778 ± 8×10^{-5}	281.088 ± 0.004	173.2158 ± 0.0002	354.00533 ± 8×10^{-5}	2456247.59
(469750) 2005 PU21	outer centaur	-	174.6 ± 0.1	0.8325 ± 0.0001	6.1748 ± 0.0001	227.856 ± 0.004	192.4938 ± 0.0003	355.7945 ± 0.0001	2456537.74
s11_good_19	outer centaur	-	205.1 ± 0.1	0.87333 ± 8×10^{-5}	26.12526 ± 5×10^{-5}	298.535 ± 0.003	148.5031 ± 0.0003	357.44987 ± 5×10^{-5}	2456888.86
2016 SG58	scattering	-	232.97 ± 0.09	0.84931 ± 6×10^{-5}	13.22082 ± 10^{-5}	296.292 ± 0.007	118.98 ± 0.0006	358.8465 ± 0.0003	2456568.8
2013 SL102	scattering	-	314.4 ± 0.2	0.87871 ± 6×10^{-5}	6.50488 ± 2×10^{-5}	265.487 ± 0.008	94.732 ± 0.001	0.2163 ± 0.0002	2456544.71
2015 BP519	scattering	-	449 ± 3	0.9215 ± 0.0006	54.1107 ± -0.0009	348.06 ± 0.01	135.2129 ± -0.0004	358.3396 ± 0.0004	2456988.83
2013 RA109	scattering	-	462.4 ± 0.4	0.9005 ± 8×10^{-5}	12.39965 ± 4×10^{-5}	262.91 ± 0.01	104.8009 ± 0.0009	0.2264 ± 0.0003	2456547.89